nature energy

Article

https://doi.org/10.1038/s41560-024-01484-z

Ion solvation kinetics in bipolar membranes and at electrolyte–metal interfaces

In the format provided by the authors and unedited

The PDF file includes:

Supplementary Notes 1-4
Supplementary Figures 1-22
Supplementary Tables 1-3
Supplementary References

Supplementary Note 1:

The absence of mass transport limitations

The results in our manuscript, in particular with regard to the increasing pre-exponential factors with bias, cannot be explained by mass transport limitations: (i) All BPMs are operated ≤ 50 mA cm^{-2} (≤ 10 mA cm^{-2} for the pristine BPM) with membranes that readily support > 1 A cm^{-2} in electrolyzers and fuel cells. (ii) All oxide-BPMs use ultra-low metal oxide loadings (0.5 - 15 µg cm^{-2}) that minimize the impact of surface ion transport over extended nanoparticle beds. (iii) The polarization curves in Fig. 1b are essentially symmetric in both directions ≤ ± 200 mV. In contrast, concentration polarization would induce asymmetric concentration profiles and polarization curves in WD and WF direction. (iv) Multiphysics simulations that match our polarization curves show negligible concentration polarization inside the junction (Supplementary Figure 18). (v) The Nyquist plots do not display any simple Warburg diffusion impedance over the whole studied potential and current range. Only at high potentials and currents for TiO_2 and SiO_2 do we observe the onset of what might be indicative of diffusion limitations (Supplementary Figure 7). (vi) Varying the amplitude (1, 5, 10 mV) during impedance measurements to test for diffusion limitations, as suggested in a recent study by Schalenbach et al.[1], does not change the results (Supplementary Figure 22). (vii) The behavior of Fig. 2c is also present at electrocatalyst interfaces at even lower currents (with reliable data starting ~ 10 µA cm^{-2}), with even sharper potential drops at concentrated electrolyte – metal interfaces (see Fig. 5d-e). (viii) Last, starting at very low current densities (<< 1 mA cm^{-2}), A and E_A increase and then saturate at higher currents and potentials, after which primarily the reduction of E_A with bias is increasing the kinetics, i.e. the kinetics start to resemble traditional Butler-Volmer kinetics (although differences remain even in that regime). Mass transport limitations, such as local pH changes, would lead to increasing deviation with increasing bias, as also discussed by others[2]. Bias dependent coverage of acid-base sites and capacitive charging of metal interfaces are fundamentally distinct from local pH changes and (bulk) transport limitations. Conversely, we refrain from assigning some of these dynamic properties to a "surface pH".

Supplementary Note 2:

Acid-base mechanism on metal oxides surfaces

Water dissociation might involve the following simplified reactions steps at acidic (a-OH/a-OH_2^+) and basic sites (b-O^-/b-OH)

$$b - O^- + H_2O \rightarrow b - OH + OH^- \text{ (R1)}$$
$$b - OH + H_2O \rightarrow b - O^- + H_3O^+ \text{ (R2)}$$
$$a - OH + H_2O \rightarrow a - OH_2^+ + OH^- \text{ (R3)}$$
$$a - OH_2^+ + H_2O \rightarrow a - OH + H_3O^+ \text{ (R4)}$$
$$a - OH_2^+ + b - O^- \leftrightarrow a - OH + b - OH \text{ (R5)}$$

The results in Fig. 2a show that E_A is minimized when the oxide's overall point of zero charge matches the local pH at the CEL. Charge neutrality of the surface then implies that either R2 and R3 or R1 and R4 (assuming similar number of sites) are coupled to dissociate water. In both cases, protons are shuttled between a large number of acidic and basic sites on the surface (R5) to

complete the cycle. A multi-site reaction mechanism with proton transport between sites has been proposed by Chen et al. previously[3]. For a point of zero charge that is much larger than the acidic local pH, all the basic groups will be strongly covered (b-OH) and most of the acidic a-OH_2^+ groups. For the few remaining a-OH groups, R3 is fast, but R4, which is needed to complete the cycle, is slow. The cycle could also be completed with a fast R1, but even less b-O^- are available than a-OH, due to an even larger difference between local acidic pH and pK_b.

The discussion above implies, that the oxide's point of zero charge and the individual pKa and pKb (related to oxide work function) not only determine the overall rate constant of each individual step, but in relation to the local pH, they also set the number of available sites and total charge at the surface. Conversely, when the local pH and point of zero charge match, charge neutrality enforces that a large configurational phase space, corresponding to 50% coverage of all acidic and basic sites, becomes available. As a result, the surface is at a state of maximum configurational entropy (Supplementary Figure 5) and coverage of a free site will lead to a small reduction of entropy and, thus, small pre-exponential factor. In contrast, an increasing difference between local pH and point of zero charge will reduce the available phase space substantially and, thus, increase the pre-exponential factor. However, the slopes between different oxides in Fig. 2a (~ 0.11 mol kJ^{-1}) are substantially lower than for the iso-current lines (~ 0.175 mol kJ^{-1}), which shows that E_A and A do not fully compensate. This implies intermediate surface coverages that are far from the extremes that would be needed to lead to sufficiently high pre-exponential factors for full compensation.

At electrochemical equilibrium, the emergence of electrostatic charge (neutrality), depending on the local pH and the oxide's work function, also links the surface configurational entropy with the configurational entropy of the water molecules. This is reminiscent of the discussion about the potential of maximum entropy for metallic surfaces. However, our results clearly show that, irrespective of the exact acid-base chemistry, the equilibrium A and E_A fall far short in describing interfacial (de)solvation comprehensively. We hypothesize that emergence of non-equilibrium (capacitive) charge at the interface leads to a decoupling of the surface configurational entropy and the entropy of interfacial water dipoles, which includes vibrational and configurational terms.

Supplementary Note 3:

Time constants from impedance spectroscopy

Maxima in the imaginary impedance, $Z_I(\nu)$, can be used to identify the time constants of individual interfacial processes ($\tau_i = (2\pi\nu)^{-1}$). For SiO_2 (Supplementary Figure 16A**)** and the other oxides (Supplementary Figure 16C-E) we observe for WD potentials slow and fast processes at $\tau_1 \sim 10^{-1} - 10^{-2}$ s and $\tau_3 \sim 5 \cdot 10^{-6} - 8 \cdot 10^{-7}$ s that we assign, consistent with our discussion in the main manuscript, to the Faradaic currents and oxide's double layer capacitance, respectively. Strikingly, for WF potentials we observe the emergence of a separate peak at $\tau_2 \sim 10^{-4}$ s for all oxides, just above the time scale characteristic of ice-structures of water ($\sim 10^{-3}$ s). For the pristine BPM (Supplementary Figure 16B) we similarly observe slow and fast processes at $\tau_1 \sim 10^{-2}$ s and $\tau_3 \sim 3 \cdot 10^{-5}$ s at WD potentials. In contrast, at WF potentials we observe a shift of the main peak to shorter times, from $\sim 3 \cdot 10^{-5}$ s to $\sim 5 \cdot 10^{-6}$ s, and a shoulder appearing again at $\tau_2 \sim 10^{-4}$ s. We hypothesize that the reduction of the total (equilibrium) electric field in the pristine BPM (Fig. 3f) shifts the main peak to smaller time constants due to a inhibition of water ordering, whereas the shoulder ($\sim 10^{-4}$ s) at higher biases for the oxide (Supplementary Figure

16A) and pristine BPMs (Supplementary Figure 16B) might be either due to (i) very slow water dynamics related to a strongly oriented shuttle water molecule at the transition state of ion (de)solvation[4], (ii) an artifact from our electrode kinetics that is absent in WD direction[5] or (iii) the accumulation of trace ions in the junction.

Supplementary Note 4:

Semi-Empirical Model for Interfacial Ion Solvation

Ordinary water auto-dissociation cannot explain BPM water dissociation. Traditionally, Onsager's 2nd Wien Effect for the conductivity of weak electrolytes[6] was applied to explain the experimentally observed BPM current densities[7]. These theories attributed exponentially increasing current densities to electric field dependent conductivity increases of a weak electrolyte (H_2O is being treated as one). As a result, the dissociation constant increases exponentially with electric fields, while the recombination rate constant remains unaffected. Later, chemical catalysis reaction models have been added to account for the observation of changing BPM activity with changing membranes or added catalysts[8]. Recently, models have been proposed to describe the catalytic rate enhancements *via* the 2nd Wien-effect, too[9]. All of these models have in common that they are unable to bridge BPMs with electrocatalysis or electrochemistry more generally. Instead, the BPM junction is treated as a unique (buried) interface which (supposedly) requires rather elaborate theory with experimentally inaccessible free parameters. For example, the (high) electric field action needs to be tuned precisely to match experimental rates.

The short-coming of 2nd Wien-effect models was also described by Hurwitz and Dibiani, who have attempted to introduce a general BPM electrochemical reaction model that appeared initially consistent with other areas in electrochemistry, such as electrocatalysis and electrodeposition[10]. Here, the reactant H_2O is being dissociated at acid-base sites inside the bipolar junction with the final product states of solvated H^+ and OH^- inside the CEL and AEL respectively. In their model, the charge transfer is described with the Butler-Volmer (BV) equation:

$$j = j_a - j_c = j_0 \left[\exp\left(\frac{\alpha F \eta}{R T}\right) - \exp\left(-\frac{(1-\alpha) F \eta}{R T}\right)\right] \quad \text{(S1)}$$

Where η is the applied overpotential with respect to the equilibrium potential, F is Faraday's constant, R is the universal gas constant in J K^{-1} mol^{-1}, T the temperature in K, α is the electron transfer coefficient (assumed 0.5), and j_0 the exchange current density that is assumed constant with bias. This approach is very similar to the one introduced by Santos and Schmickler[11]for reactions involving ion (de)solvation, such as during electrodeposition. In these models, the free energy of the electron (in the traditional outer-sphere B-V equation) is exchanged with the free energy of the ion in solution. As outlined in the introduction of the Main Text, 2D free energy surfaces are calculated dependent on the degree of solvation and distance from the (static) solid-electrolyte interface with the help of (equilibrium) DFT[12]. Under bias, the free enthalpy of the solvated proton is shifted by the applied potential. As noted by Pecina and Schmickler, this theory is incomplete when part of the bias (reversibly) changes interfacial capacitance that could induce water reorientation during the solvation transition state[4]. Under these conditions, traditional Butler-Volmer theory cannot explain catalyst kinetics, neither in in electrochemistry nor in BPMs.

Due to the limitations of previous theories, we consider that the generation/recombination of ions during water dissociation and water formation in the presence of ionogenic groups will require the reorganization of the solvation spheres to enable the interfacial ion transport in the presence of an electrostatic potential drop. For didactic purposes, in the first step the mathematical description of these processes can still be considered as a slightly modified form of the BV equation for water dissociation and water formation:

$$j = j_{WD} - j_{WF} = c_{H_2O}\, k_{WD}\, \exp\left(\frac{\alpha_{WD}\, F\, \eta}{R\, T}\right) - c_{OH^-} c_{H^+}\, k_{WF} \exp\left(-\frac{\alpha_{WF}\, F\, \eta}{R\, T}\right) \qquad \text{(S2)}$$

Where α_{WD}/α_{WF} are the ion transfer coefficients and they do not need to be 0.5 since they are simply experimentally obtained parameters (more below). Note that the j_0 terms have been expanded into their respective chemical kinetic expression where k_{WD}/k_{WF} are the kinetic constants and c_{H_2O}, c_{OH^-}, and c_{H^+} are the concentrations of water, hydroxide, and protons respectively. The kinetic constants can be further expressed in terms of the transition's state apparent activation energy (E_a) and the Arrhenius pre-exponential factor (A_{WD}/A_{WF}):

$$\begin{aligned} j = {} & c_{H_2O} A_{WD}(\eta) \exp\left(-\frac{E_{A_{WD}}}{RT}\right) \exp\left(\frac{\alpha_{WD}\, F\, \eta}{R\, T}\right) \\ & - c_{OH^-} c_{H^+}\, A_{WF}(\eta) \exp\left(-\frac{E_{A_{WF}}}{RT}\right) \exp\left(-\frac{\alpha_{WF}\, F\, \eta}{R\, T}\right) \end{aligned} \qquad \text{(S3)}$$

Our experimental results clearly demonstrate that E_a and A are both bias dependent and reflect bias-dependent enthalpic and entropic contributions, respectively (e.g. Fig. 2 or Fig. 5). For this reason, we choose to treat α in S1 as a general charge transfer coefficient. This was also suggested for electrocatalysis[13,14], to refrain from overinterpreting seemingly constant Tafel slopes, with somewhat limited success given current electrocatalyst literature. To contrast and deconvolute the traditional α, we introduce two separate parameters, γ and σ, each one expressing the respective susceptibility of A and E_a to the applied bias, respectively. Currently, the exact analytic form of A(η) is unknown. Our experimental results and comparison with literature suggests an approximate form for $\Delta \log \mathrm{A} \sim \mathrm{a} \cdot \log_{10}(\eta) + \mathrm{b}$ (Fig. 5). Therefore, as a first approximation we describe it with a linear dependency on η:

$$\begin{aligned} j = {} & c_{H_2O}\left(A_{0_{WD}} + \gamma_{WD}\, \eta\right) \exp\left(\frac{-E_{A_{WD}} + \sigma_{WD}\, F\, \eta}{R\, T}\right) \\ & - c_{OH^-} c_{H^+} \left(A_{0_{WF}} - \gamma_{WF}\, \eta\right) \exp\left(\frac{-E_{A_{WF}} - \sigma_{WF}\, F\, \eta}{R\, T}\right) \end{aligned} \qquad \text{(S4)}$$

with A_0 and E_a being the pre-exponential factor and activation energy at equilibrium, respectively. This general equation captures the essence of our interfacial solvation model.

Our approach has some similarities to the one recently discussed by Chen et al.[3]. There, increasing pre-exponential factors with constant activation energies have been observed for a single TiO_2-catalyed BPM junction biased in WD direction. As a result, the authors proposed a linear dependence of the pre-exponential factor with WD overpotential for WD currents. However, a

more comprehensive ion (de)solvation model (including the reverse rate), the link to interfacial capacitance, electrocatalysis and simulation results were not discussed.

For implementation in a Multiphysics simulation, we also need to consider the equilibrium concentrations of c_{OH^-} and c_{H^+}, which are set to the auto-protonation of water, whereas c_{H_2O} is set to the unit activity:

$$j = \left(A_{0_{WD}} + \gamma_{WD}\,\eta\right)\exp\left(\frac{-E_{A_{WD}} + \sigma_{WD}\,F\,\eta}{R\,T}\right) - \frac{c_{OH^-}c_{H^+}}{K_w}\left(A_{0_{WF}} - \gamma_{WF}\,\eta\right)\exp\left(\frac{-E_{A_{WF}} - \sigma_{WF}\,F\,\eta}{R\,T}\right) \quad \text{(S5)}$$

where K_w is the auto-dissociation constant of water (10^{-8} mol^2 m^{-6} at 25ºC). According to our results in Fig. 4a, free recombination of protons and hydroxide ions inside the junction would increase the WF currents too fast. For this reason, a simple Langmuir-type expression is introduced to account for the coverage of the available catalytic sites contributing to WF currents:

$$\theta = 2\frac{\left(\frac{c_{OH^-}c_{H^+}}{K_w}\right)^n}{1 + \left(\frac{c_{OH^-}c_{H^+}}{K_w}\right)^n} = 2\frac{{c_{term}}^n}{1 + {c_{term}}^n} \quad \text{(S6)}$$

where n is a parameter that determines the coverage profile and is kept by default as 1. We note, that more experimental studies are needed to dissect whether Langmuir or other adsorption behavior is present on the metal oxide surfaces when operated at WF potentials.

At electrochemical equilibrium, BPM junctions possess an electrostatic potential drop due to the difference of activity of protons and hydroxides in the CEL and the AEL (compare to the equilibrium electric field in semiconductor p-n-junctions). For protons, the activity in the CEM is high and low in the AEM and *vice versa* for hydroxides. At electrochemical equilibrium, the electrochemical potential ($\bar{\mu}_i$) across the BPM junction is constant[15] and an electrostatic drop appears to balance the chemical potential difference:

$$\phi_{BPM_{eq}} = \phi_{CEM} - \phi_{AEM} = \frac{RT}{F}\ln\left(\frac{a_{H^+}^{AEM}}{a_{H^+}^{CEM}}\right) \approx 59\ (mV) \times \Delta pH \quad \text{(S7)}$$

For an AEM with 1M OH$^-$ (10^{-14} M H$^+$) and a CEM with 1M H$^+$ this drop corresponds to ~ 830 mV. The drop manifests itself as an equilibrium electric field in the BPM junction (E_0). The final expression for ionic solvation model is obtained by substituting the overpotential dependency of equation S5 by the effective electric field ($E_{eff} = E - E_0$) which leads to a microscopic description of the potential drop in the BPM junction:

(S8)

$$j = \left(A_{0_{WD}} + \gamma_{WD}\, E_{eff}\right) \exp\left(\frac{-E_{A_{WD}} + \sigma_{WD}\, E_{eff}}{R\,T}\right) - \theta\left(A_{0_{WF}} - \gamma_{WF}\, E_{eff}\right) \exp\left(\frac{-E_{A_{WF}} - \sigma_{WF}\, E_{eff}}{R\,T}\right)$$

j is finally expressed in terms of a chemical reaction rate to be used in the Multiphysics simulation describing the generation/consumption of ionic carriers:

$$R\ [mol\ m^{-2}] = \frac{j}{l_{junction} F} \quad \text{(S9)}$$

Where $l_{junction}$ is the junction thickness. This semi-empirical model captures the essence of interfacial ion (desolvation) in the BPM and electrochemistry in general. In contrast to conventional models, the Arrhenius pre-exponential factor is left bias dependent, resulting in a simpler, less parametrized model and instead leverages experimentally determined parameters. See Supplementary Table 2 for the models' equations.

Semi-Empirical Model Parametrization and Validation

The kinetic parameters of our model (equation S8) were extracted from temperature dependent studies. For a BPM with 23 µg cm^{-2} of TiO_2-P25 the E_{a0} is estimated for overpotentials close to equilibrium to be 21 kJ mol^{-1} (Supplementary Figure 2). Compared to the experimental determination of E_{a0}, extracting $A_{0,WD}$ and $A_{0,WF}$ is more challenging, as the experimental data only informs on the total A, i.e. $A_{0,WD}$ - $A_{0,WF}$ for WD potentials. Due to the high exchange current densities observed, we cannot *a priori* assume strongly suppressed reverse rates, as is commonly done for Butler-Volmer-based theory. Instead, $A_{0,WD}$ was estimated from the logarithmic saturation far away from equilibrium (as shown by $\log_{10}$A in Fig. 5) to be around $10^{5.5}$ mA cm^{-2}. The j_0 corresponding to this A and E_a at 25ºC is close to 140 mA cm^{-2}, consistent with previous reports that indicated that WD catalysts stay in their reversible regime for ≥100 mA cm^{-2} [3,10] and our results, with linear polarization curves (Fig. 1) and constant E_A (Fig. 2). The susceptibility parameters to the electric field, γ and σ, were estimated by correcting the variation of A and E_a with overpotential by a junction thickness of 20 nm (a monolayer of P25-TiO_2) and assuming a linear variation of A and E_A in the range of ~ 0 to 200 mV for WD potentials. To avoid over-parametrizing the model, the susceptibilities of WD and WF were kept identical. The change in A is estimated to be 0.03 S m^{-1} (multiplied by the electric field [V m^{-1}] results in [A m^{-2}]) and the change in E_A to be $5{\cdot}10^{-5}$ m C mol^{-1} (multiplied by the electric field results in [J mol^{-1}]). These susceptibilities were used to compare the experimental current densities obtained with the simulated ones (Fig. 4), resulting in a close approximation and informing on the concentration profile of ionic carriers in the BPM junction (Supplementary Figure 18A) as well as for the magnitude of the electric field (Supplementary Figure 18B). Different junction sizes and their impact on the simulated current-voltage curves were also tested showing a change of the effective electric field (Supplementary Figure 18 C-D) which is used by our model. Due to the simplified potential drop and electric field distribution across the junction, changing the junction dielectric constant does no impact the kinetics (Supplementary Figure 19A). Moreover, A_0, γ, and σ were validated by testing a range of values for each of them (Supplementary Fig. 19B-C) leading to qualitatively similar polarization curves while staying quantitatively in the range of the experimental results. Unless stated otherwise, the parameters used for each simulation are shown in Supplementary Table 2.

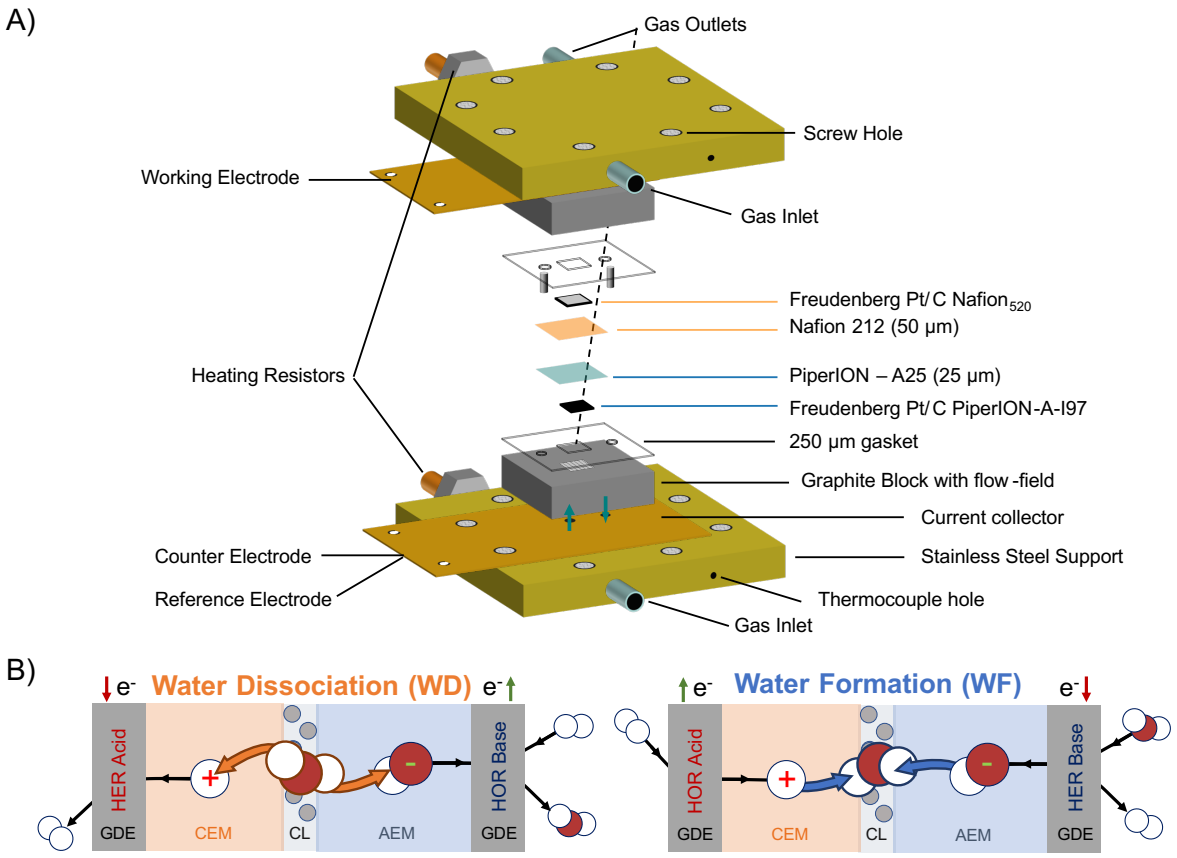

Supplementary Figure 1. Bipolar Membrane Assembly and Interfacial Water Dissociation and Formation. A) The zero-gap membrane electrode assembly (MEA) enables electrochemical operation that fully relies on ion-conducting polymer membranes (Nafion as cation-exchange layer and PiperION as anion-exchange layer) for ionic conductivity. As a result, the system can be operated with pure water humidified gases in a fuel cell mode. The continuous compression enables not only careful control between gas diffusion electrodes and polymer membranes, but also of the bipolar junction between the membranes. **B)** Interfacial water dissociation and formation ($H_2O \leftrightarrow H^+ + OH^-$), involving H^+ and OH^- solvation and desolvation, respectively, are driven controllably inside the bipolar junction by driving HER and HOR reversibly on the humidified gas diffusion electrodes.

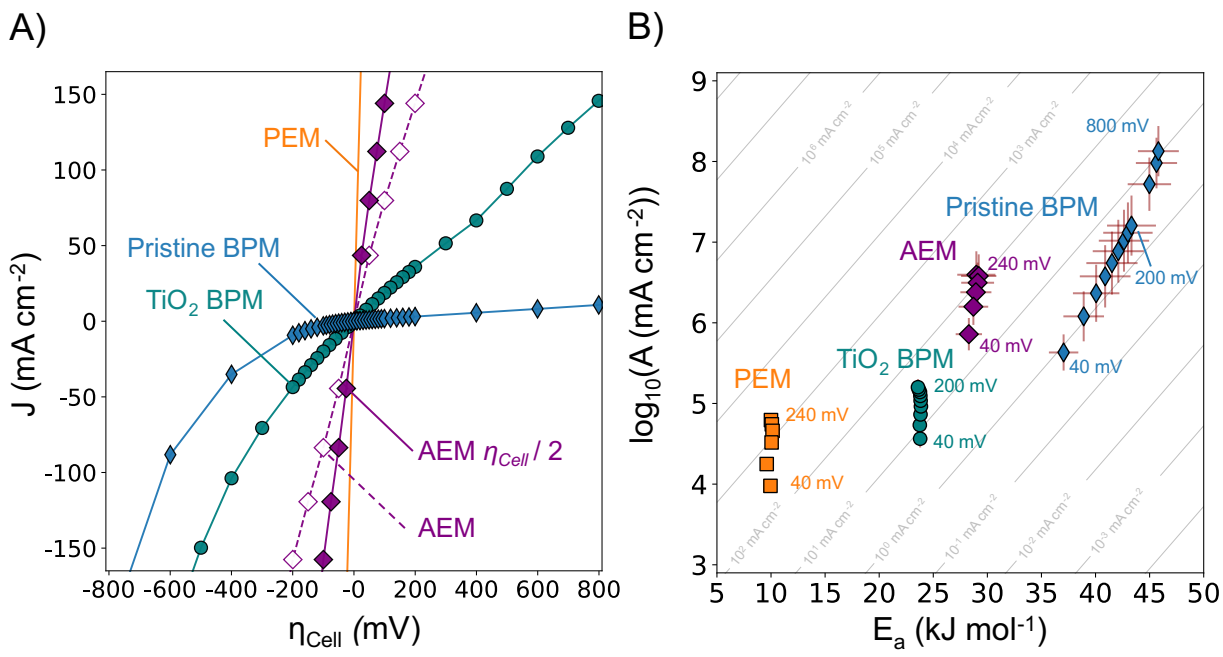

Supplementary Figure 2. PEM and AEM Reference Measurements. A) Polarization curves for the PEM and AEM reference systems compared with a pristine BPM and one containing 2 µg cm^{-2} TiO_2-P25. All membranes were operated with 2 mg cm^{-2} Pt/C GDEs (with respective ionomers). When using a BPM-MEA, one electrode runs the HER/HOR reactions at acidic pH (CEL interface) and the other at alkaline pH (AEL interface). The PEM and AEM reference H_2-H_2 fuel operate the HER and HOR at the same acidic or alkaline pH, respectively. Whereas the kinetics of the acidic HER/HOR lead to a very low overpotential for the CEM reference, the slower kinetics for the alkaline HER/HOR give rise to a noticeable overpotential (at comparable current densities). However, in the BPM, only one electrode is operated in alkaline conditions, therefore the overpotential contribution from the alkaline HER/HOR is cut into half. Overall, the overpotentials are substantially lower than for the BPM-MEAs, even when using TiO_2-P25. **B)** E_A and A with iso-current lines calculated at 65ºC (background grey lines). The low current density and potential range studied here (0.1-50 mA cm^{-2}) ensures that the extracted E_A and A are stemming from the bipolar junction and are not the high loading electrodes. We refrain from interpreting A and E_A qualitatively for the high current density and high loading PEM and AEM reference cells. In contrast to the BPMs with a sharp junction and operated at much lower current densities and low loadings, the reference systems are impacted by mass transport limitations in the extended gas diffusion electrodes, surface ion transport and potentially local pH changes in the GDEs. Error bars measured with the standard error in the slope (E_a) and intercept ($\log_{10}$A) of the Arrhenius linear regression with 5 samples (temperatures).

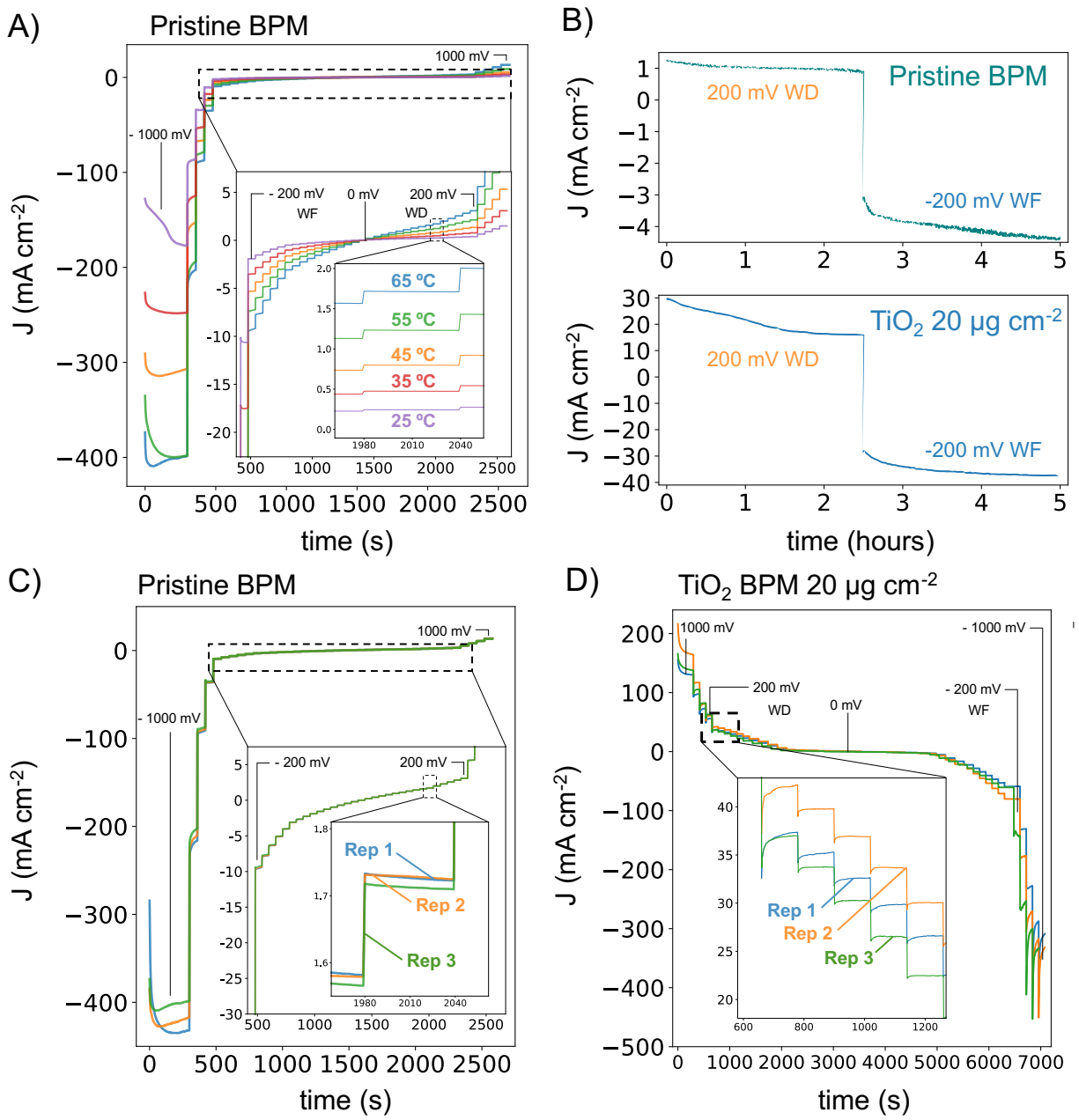

Supplementary Figure 3. Reproducibility and Stability of the BPM-MEAs. A) Chronoamperometry of a pristine BPM during temperature-dependent measurements. For the investigated range of ± 200 mV no unstable performance was observed. **B)** Chronoamperometry with individual potential holds of 2.5h for a BPM with TiO_2-P25 and a pristine BPM. For the TiO_2-BPM a small decrease in performance is observed for WD during 2.5 hours, while the WF performance slowly rises during the subsequent potential hold. Please note that the temperature dependent changes **(A)** are substantially larger than this small performance variation. **C)** Reproducibility for three freshly prepared pristine BPMs at 65 ºC. **D)** Reproducibility of a BPM with three 20 µg cm^{-2} TiO_2 BPMs at 65ºC, which is used to calculate the error bars for the experimental curves in Fig. 4.

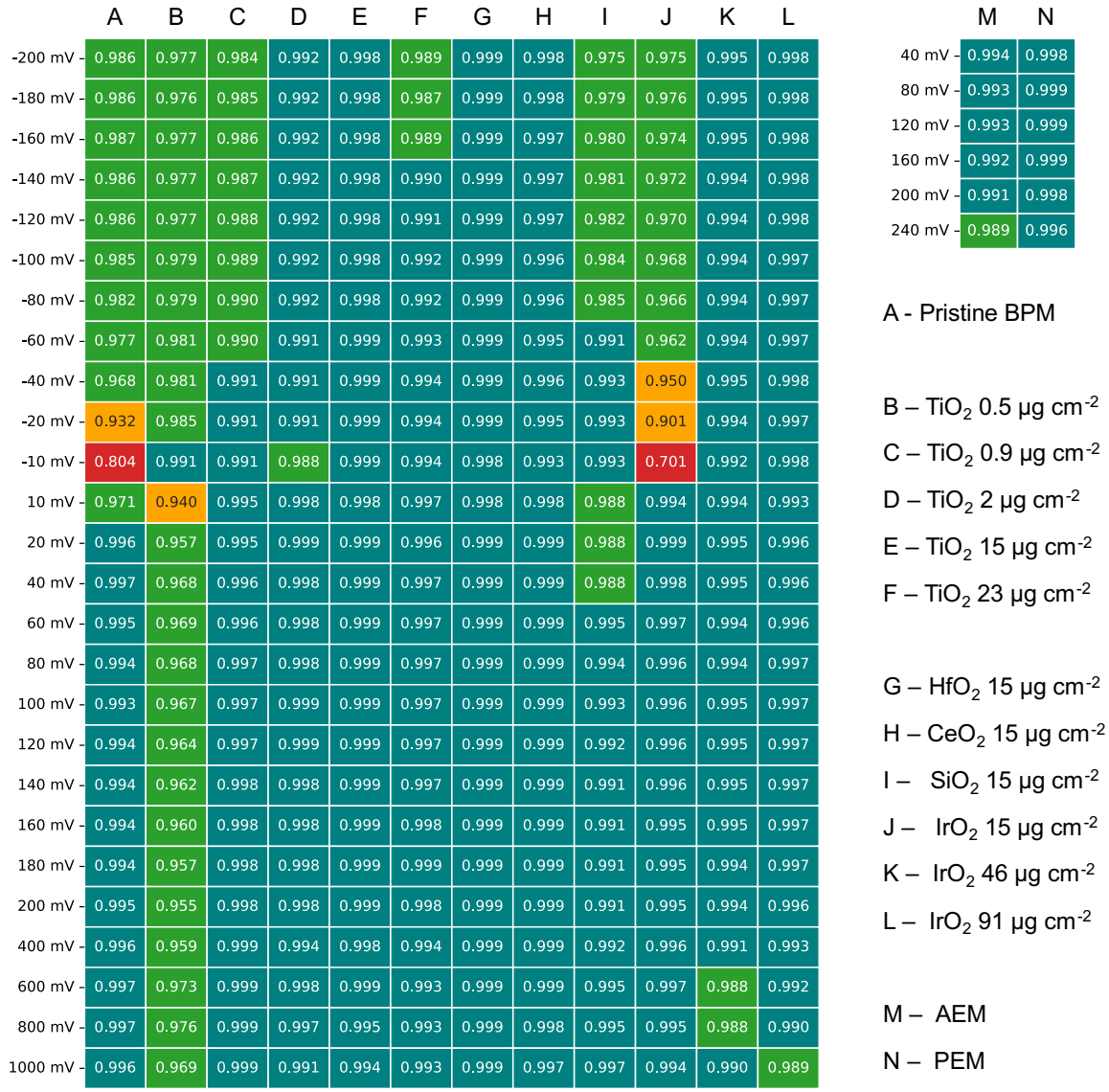

Supplementary Figure 4. Heatmap for all R^2 values from the linear MEA Arrhenius fits. The R^2 value for all WD potentials (positive values) is generally kept well above 0.95, ensuring high accuracy of the reported E_A and A values. For WF potentials, the errors are slightly higher. In general, due to the changing concentrations of protons and hydroxides during WF, the WF rates do not directly inform on E_A and A, in contrast to the constant H_2O concentration during WD currents ($\leq$ 50 mA cm^{-2}). The colors in the table help emphasize the degree of confidence of the extracted A and E_A. The number of samples (temperatures) for each regression is 5.

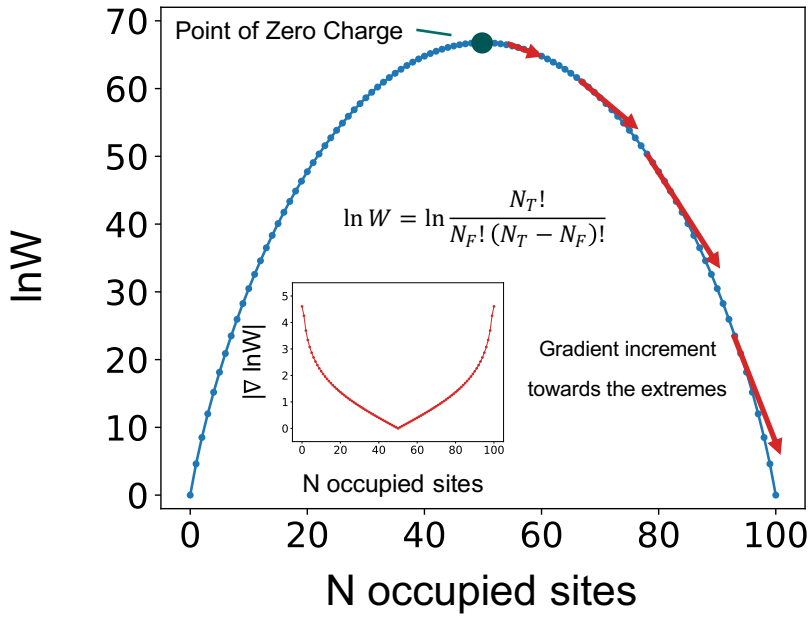

Supplementary Figure 5. Configurational surface entropy. The maximum of the configurational entropy is reached for 50% coverage of all available (total) sites (N_T). Thus, with decreasing or increasing coverage (free sites N_F) the configurational entropy is reduced. Importantly, the incremental decrease in configurational entropy increases with increasing and decreasing initial coverage (inset).

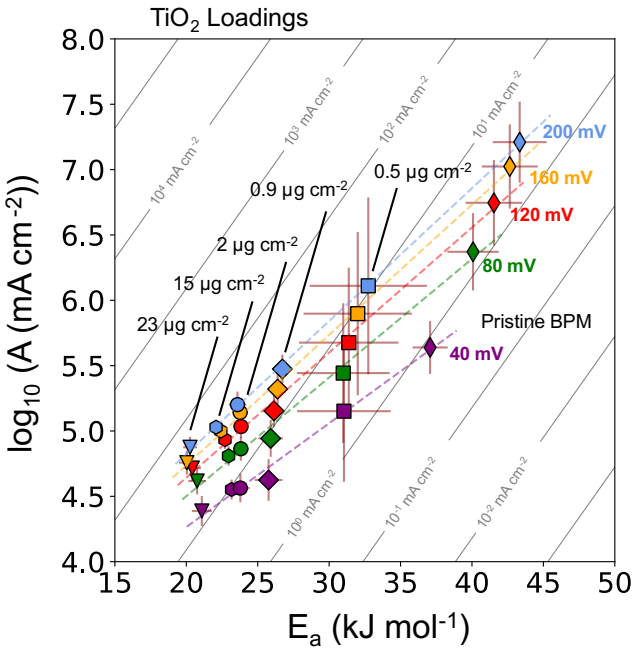

Supplementary Figure 6. Entropy-enthalpy relationships for additional TiO_2 catalyzed BPM loadings. At ultra-low loadings of around 2 µg cm^{-2} the activation energy stays essentially constant with potential. For larger loadings, the activation energy slightly decreases with bias. However, for these loadings the kinetics might be impacted by activated ion surface transport over the extended nanoparticle beds and the total current densities get closer to the reference AEM and PEM. Irrespective, the increasing currents are primarily caused by increasing pre-exponential factors, especially at lower bias. For the discussion about the loadings < 2 µg cm^{-2} see discussion in main manuscript. Error bars measured with the standard error in the slope (E_a) and intercept ($\log_{10}A$) of the Arrhenius linear regression with 5 samples (temperatures).

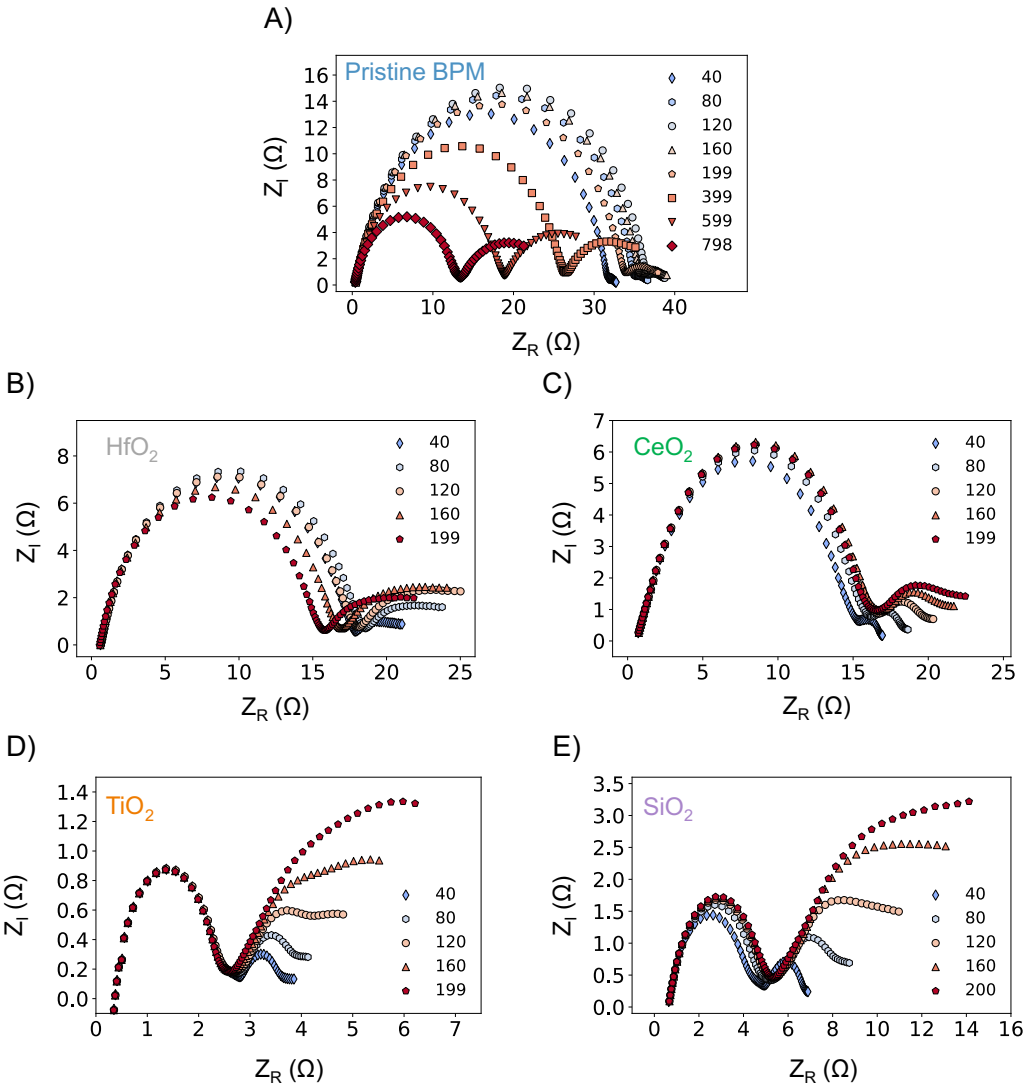

Supplementary Figure 7. Nyquist plots for pristine and metal oxide catalyzed BPMs. A) For the pristine BPM, and low WD bias, the Nyquist plot is dominated by a single semi-circle, almost over the whole frequency range. At biases > 200 mV and lower frequencies, a second semi-circle appears that we assign to the build-up of membrane space charge (see Supplementary Figure 16 for time constants). Noteworthy, the semi-circular shape is clearly evident and contrasting diffusion-related Warburg elements which appear in Nyquist plots as a straight line with a 45° angle to the x-axis. **B, C)** Nyquist plots for HfO_2 and CeO_2 with qualitatively similar behavior as the pristine BPM, except for near constant charge transfer resistance. **D, E)** Nyquist plots for TiO_2 and SiO_2 that show qualitatively similar behavior to HfO_2 and CeO_2 at low potentials (and current densities) and increasingly deviating behavior at higher potentials. Especially at potentials ≥ 160 mV, we observe an increasing linear feature at lower frequencies that might be attributed to transport-related changes during bias dependent deprotonation and dihydroxylation in the membrane's space charge region. However, it only appears at low frequencies and high bias (and current densities) and strongly contrasts the impedance of all other BPMs. Therefore, such (potentially) mass transported related processes cannot explain the trends discussed in the main paper.

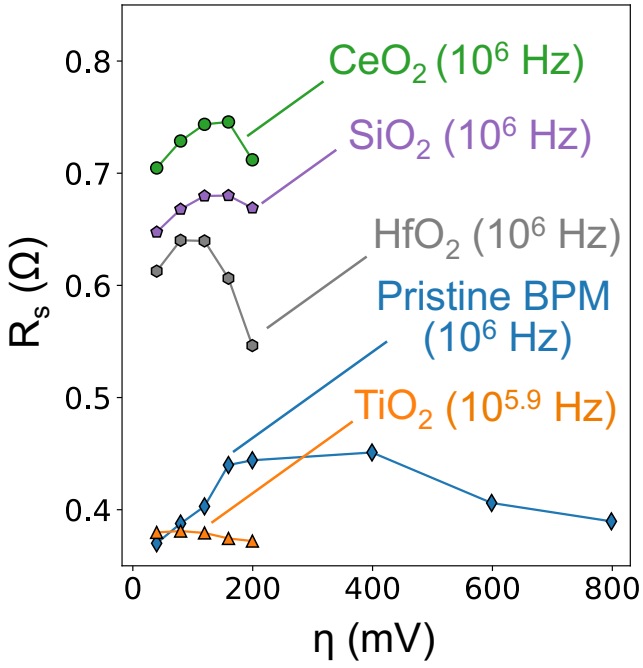

Supplementary Figure 8. High frequency series resistance for BPM-MEAs. The high frequency resistance of all BPM-MEAs is low, confirming proper zero-gap assembly with low ionic and electrical resistances. Noteworthy, the low series resistance enables us to extract capacitance reliably even at high frequencies up to 500 kHz (see high frequency tails in the Nyquist plots in Supplementary Figure 7).

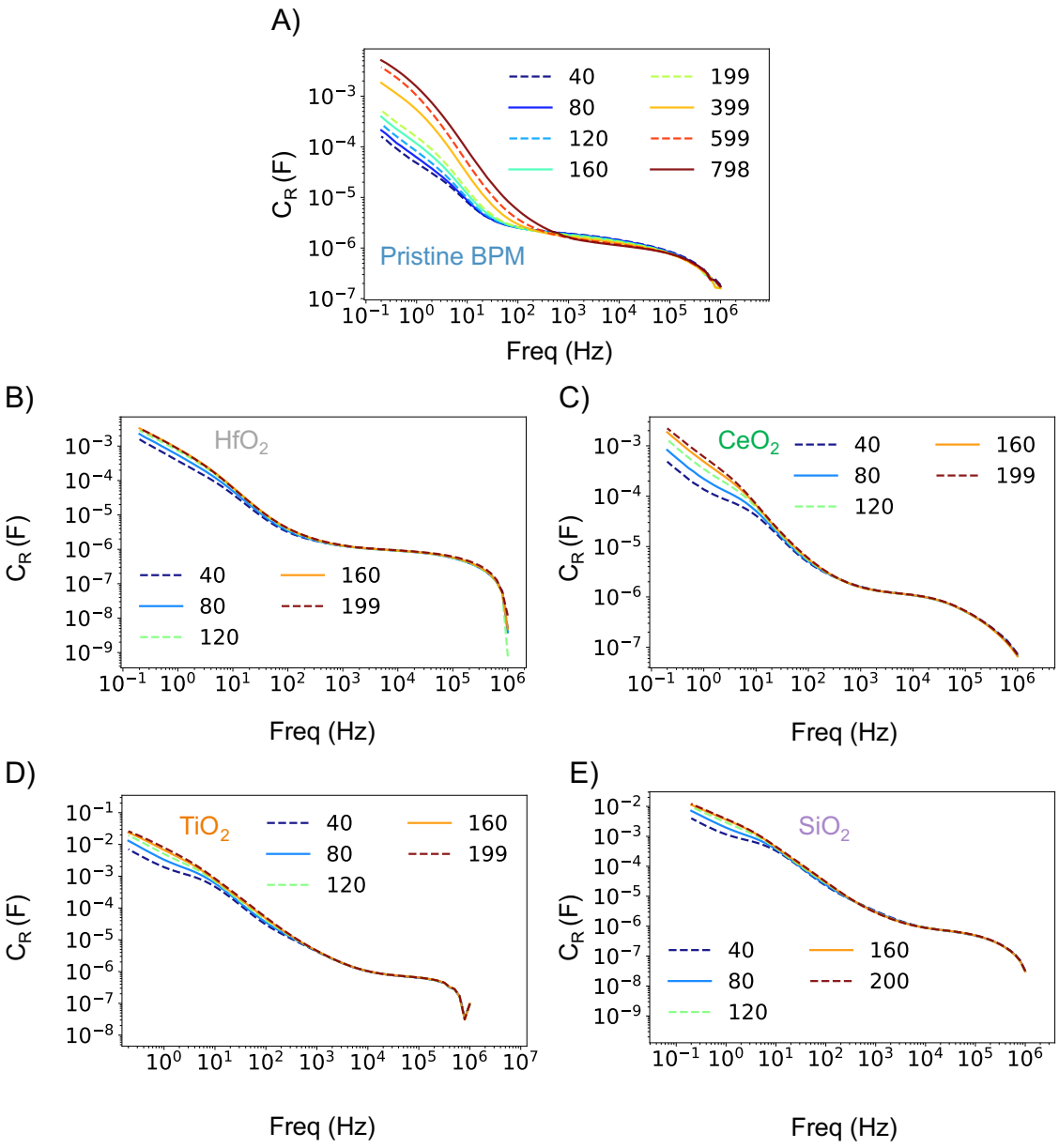

Supplementary Figure 9. Real capacitance Bode plots for pristine and metal oxide BPMs. A) The real part of the capacitance $C_R(\omega) = -Z(\omega)_I \cdot (\omega \cdot |Z(\omega)|^2)^{-1}$ for the pristine BPM displays clear bias dependent features (see also Supplementary Figure 10). Note, even at or close to equilibrium the capacitance increases with lower frequencies. Such impedance behavior is not caused by mass transport limitations (see Supplementary Note 1) and discussion by Schalenbach et al.[1]. **B-E)** The real capacitance for the HfO_2, CeO_2, P25-TiO_2, SiO_2 all displays bias dependent features at lower frequencies < 1kHz. However, in contrast to the pristine BPM, no bias dependent changes are apparent at higher frequencies 1kHz-1MHz.

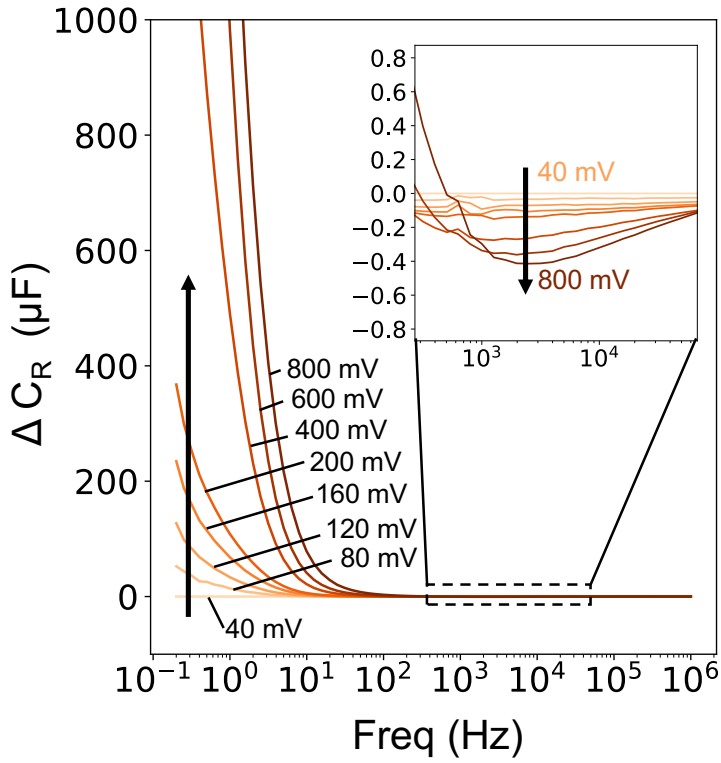

Supplementary Figure 10. Bias dependent changes of the real capacitance with respect to 40 mV. For the pristine BPM we observe that changes in the real capacitance at low frequencies (≤ 100Hz) are correlated with changes at high frequencies (~ 1kHz-1MHz). This indicates that the different processes occurring at different time scales (Supplementary Figure 16) and are electrostatically coupled at the interface.

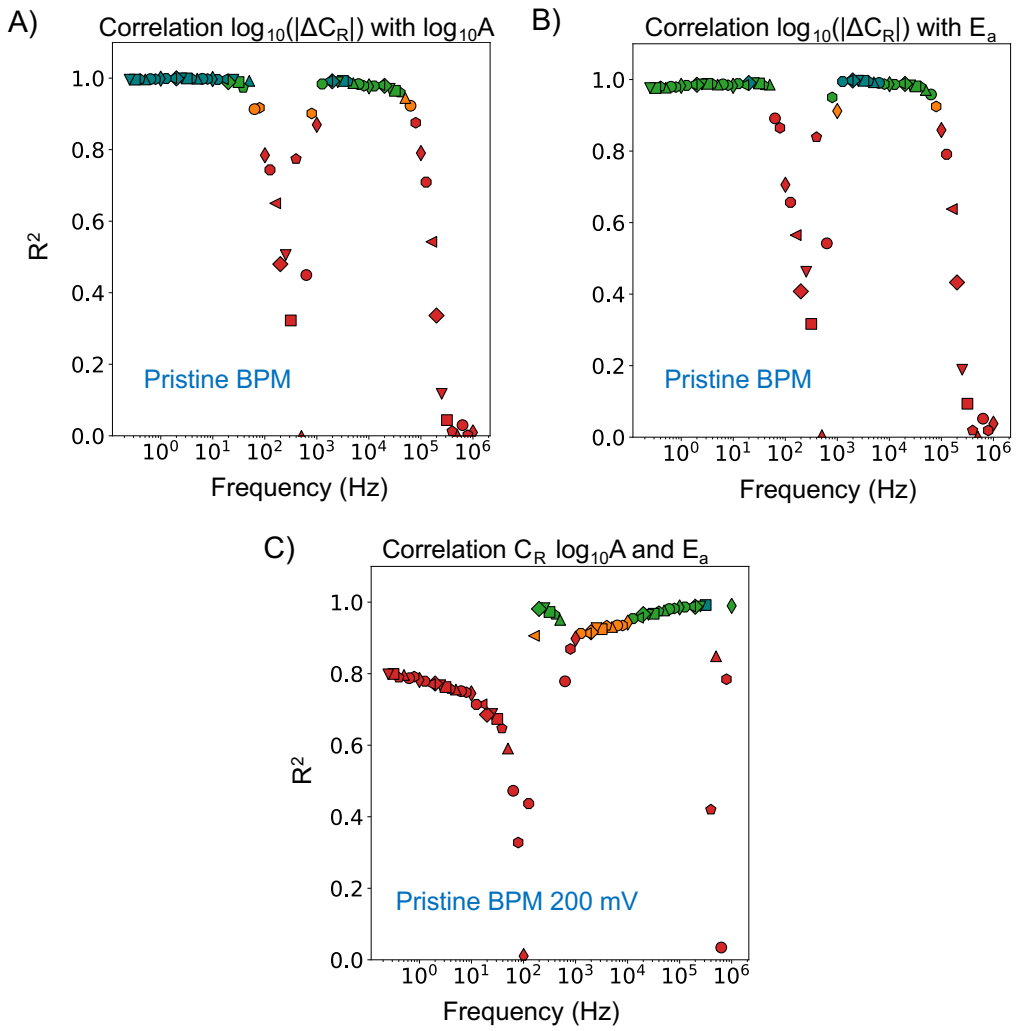

Supplementary Figure 11. Correlation of real capacitance with Arrhenius parameters for the pristine BPM. A, B) Close correlations (R ~ 1) of real capacitance changes with bias ($\log|\Delta C_R|$) with $\log A$ and E_a up to 800 mV for the pristine BPM. Due to the ideal correlation between log A and E_A discovered in Fig. 2C, $\log A$ and E_a correlate in the same manner with $\log|\Delta C_R|$ (see also Supplementary Figure 13). C) When we correlate $\log A$ and E_a with C_R, instead of $\log|\Delta C_R|$, we find correlations at higher frequencies (100kHz-1MHz) up to 200 mV. With the help of the results of the oxides (below), we are able to dissect the contributions and can assign the high frequency correlations of C_R to changes in E_a, whereas the low frequency correlations of $\log \Delta C_R$ are linked to logA.

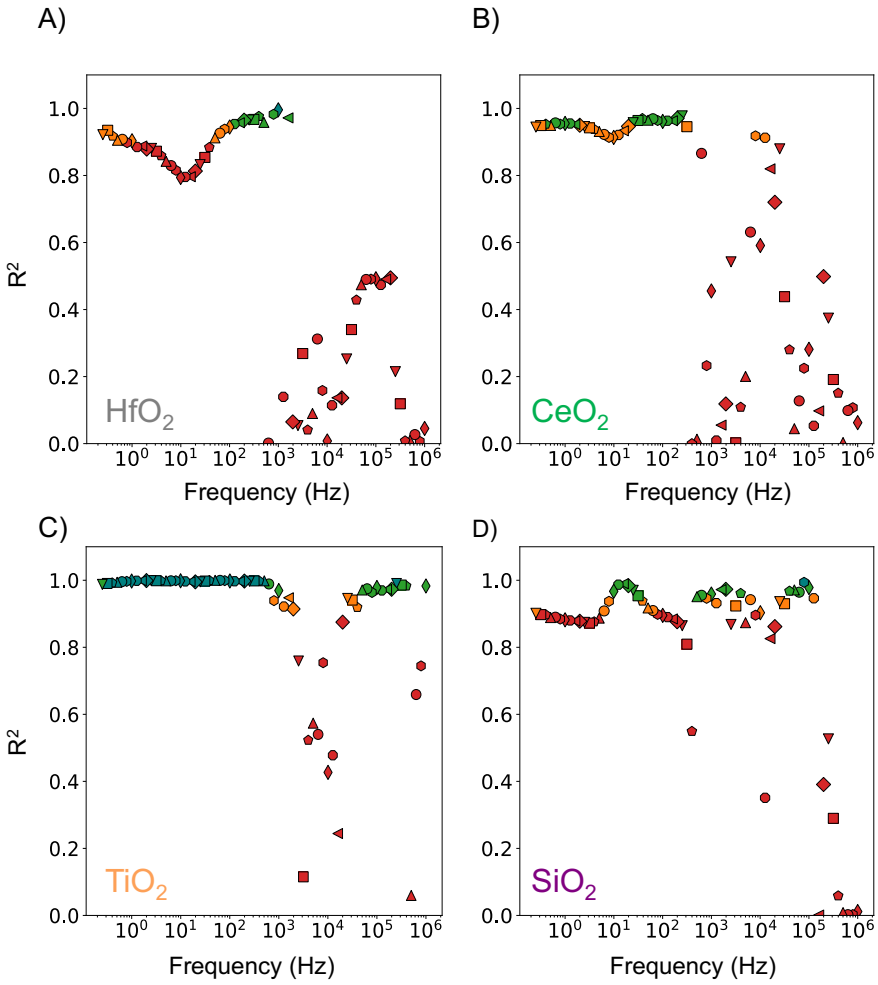

Supplementary Figure 12. Correlation of log (|ΔC_R|) with log A for the metal oxide BPMs. A-D) For all oxide catalyzed BPMs we find close correlations (R ~ 1) of log (|ΔC_R|) at lower frequencies ≤ 100 Hz with log A. Compared to the pristine BPMs, there are no extended frequency bands with R ~ 1 apparent at higher frequencies, except for the TiO_2 catalyzed BPM. We ascribe this to the near constant activation energies with bias for the oxide-catalyzed BPMs in Fig. 2. Instead, the increasing rates are primarily driven by increasing pre-exponential factors, which correlate with low frequency capacitances. We ascribe the latter to slow deprotonation and dehydroxylation reactions inside the membranes space charge region at Faradaic WD potentials and frequencies. These reactions are the origin of bias dependent space charge and the capacitive electric fields.

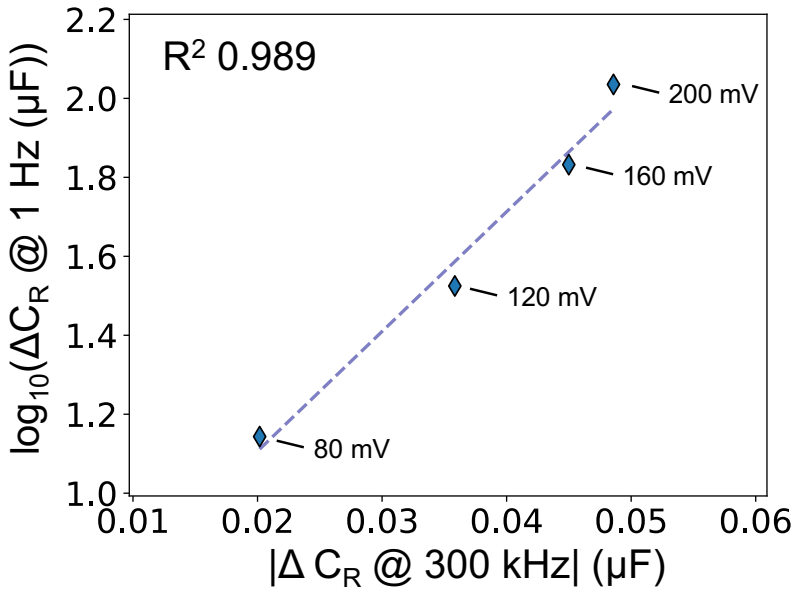

Supplementary Figure 13. Direct capacitance correlation for pristine BPM. Due to the close correlation found in Fig. 2C between $\Delta\log_{10}$ and ΔE_A (B), the respective capacitances at low and high frequencies also correlate strongly. This correlation can be understood by electrostatic coupling between the bias dependent acid-base sites coverage and the build-up of capacitive electric fields that change the reaction's thermal entropy. The very acid-base sites that catalyze the reaction are also responsible for establishing the capacitive electric fields.

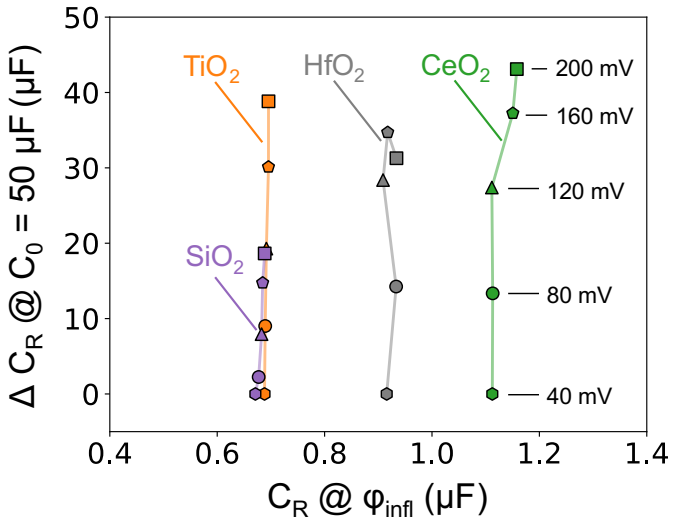

Supplementary Figure 14. Change of $log_{10}A$ with C_R at the inflection point of the phase angle for metal-oxide BPMs. Except for the SiO_2 the results are very similar to the ones in Fig. 3C. This can also be understood by considering Fig. 3A. With increasing frequencies, the correlation of C_R with E_A becomes more linear, which leads to better separation in Fig. 3C compared to here. This finding might imply that E_A is fundamentally linearly instead of logarithmically related to C_R at high frequencies.

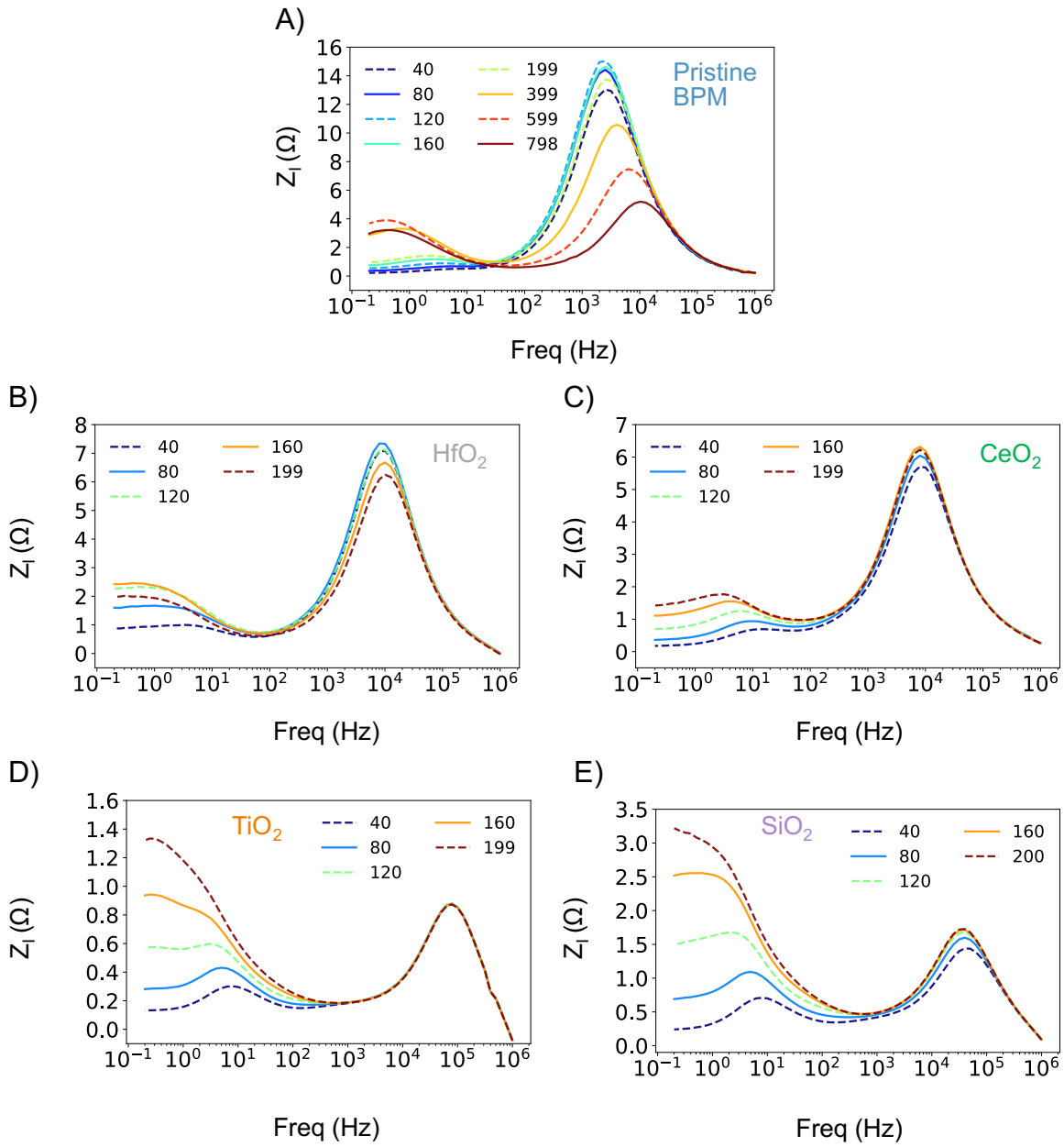

Supplementary Figure 15. Imaginary impedance of pristine and metal oxide BPMs. A) Imaginary impedance of pristine BPM (for discussion see Main Text). B-D) Bias dependent imaginary impedances of oxide-catalyzed BPMs that all show similar features. The main peak at high frequencies barely changes with bias and can be assigned to constant activation energies and time constants due to constant acid-base chemistry. However, the low frequency peak shifts toward lower frequency and thus higher time constants. As discussed above and in the Main Text, we assign this peak to capacitive processes during Faradaic turn-over. Compared to the pristine BPMs, the membrane's acid-base sites are electrostatically decoupled from the oxide's surface chemistry and high frequency capacitance. As a result, the high frequency peak remains unchanged. In stark contrast, for the pristine BPM, the catalytically active acid-base sites are intimately involved in establishing the non-equilibrium electric fields, which leads to changes of the high frequency peak and activation energy, which are discussed in the Main Text.

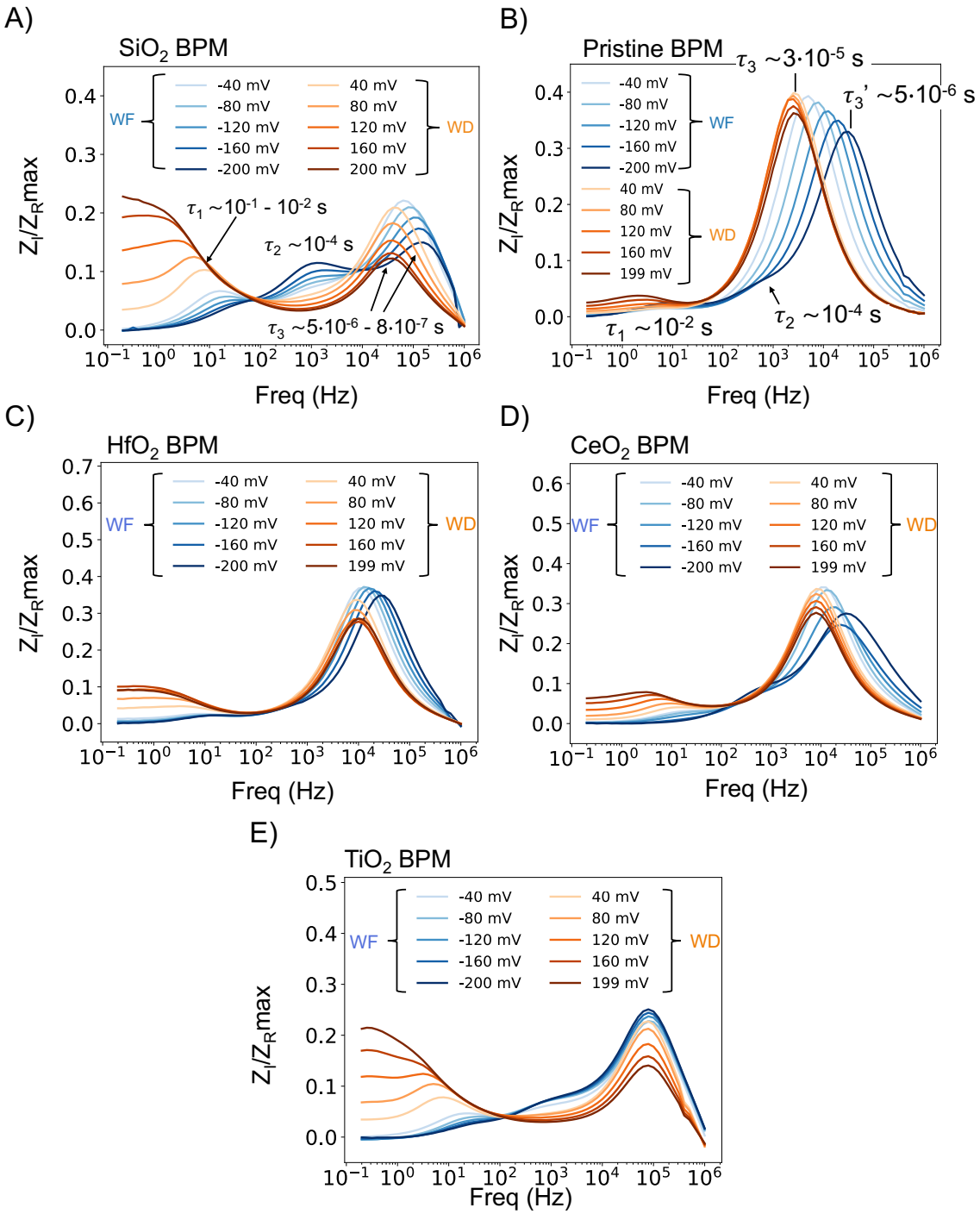

Supplementary Figure 16. Normalized impedance for pristine and oxide-catalyzed BPMs. (A) The imaginary part of the impedance, $Z_{im}(\nu)$, normalized by the resistive maximum of the real part, $Z_r(\omega)$, shows for the SiO_2 BPM three distinct peaks for water formation potentials with time constants ($\tau_i \sim (2\pi\nu)^{-1}$), which we ascribe to Faradaic current ($\tau_1 \leq 10^{-2}$ s), double layer capacitance ($\tau_3 \sim 10^{-6}$s) and tentatively to strong water ordering and/or ion accumulation ($\tau_2 \sim 10^{-4}$s). (B) For WF potentials and the pristine BPM, we observe a double layer capacitance shift from $\tau_3 \sim 3 \cdot 10^{-5}$ s to $\tau_3' \sim 3 \cdot 10^{-6}$ s and a shoulder at $\tau_2 \sim 10^{-4}$ s, as for the oxides. We

assign the high frequency peak shift to changes in the protonation and hydroxylation state of the polymer groups. For WD potentials, the τ_2 is absent and we only observe the τ_1 and τ_3 peaks, potentially because the impedance at these time constants might be dominated by the equilibrium electric field or the absence of ion accumulation. C-E) Normalized impedance for HfO_2, CeO_2 and TiO_2.

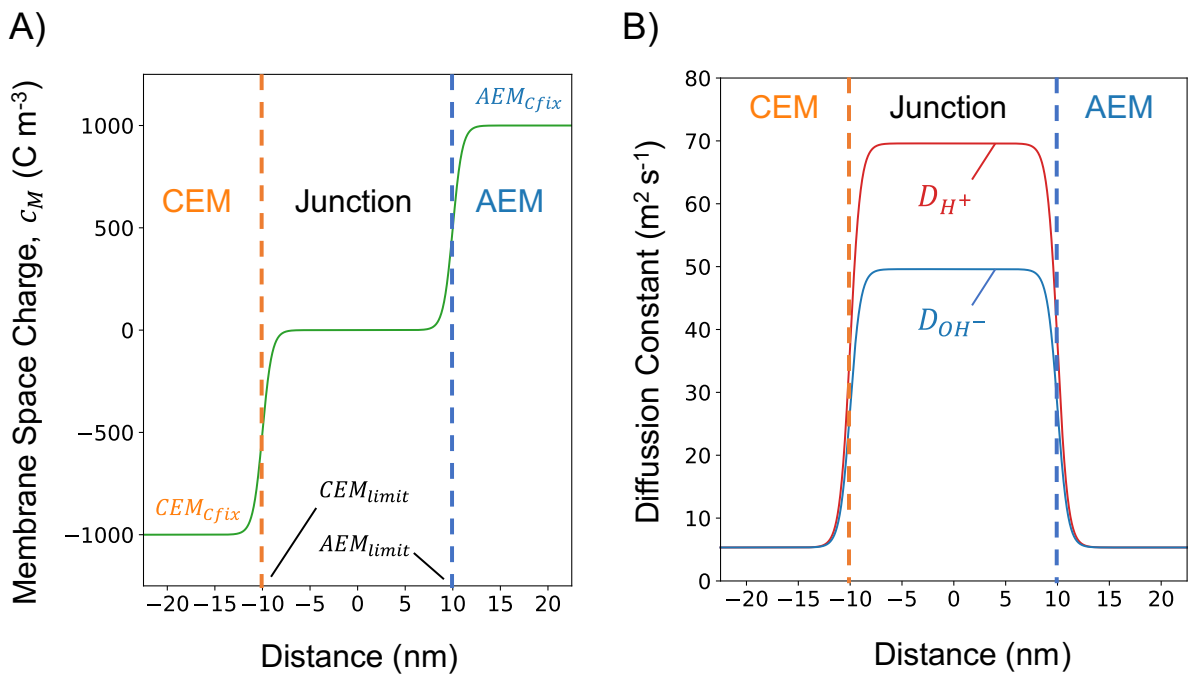

Supplementary Figure 17. Setup of COMSOL domains. The membrane space charge (A) and the diffusion constants (B) were described by hyperbolic tangents that ensure smooth transitions at the domain boundaries. For details about the model and parameterization see Methods and Supplementary Note 4.

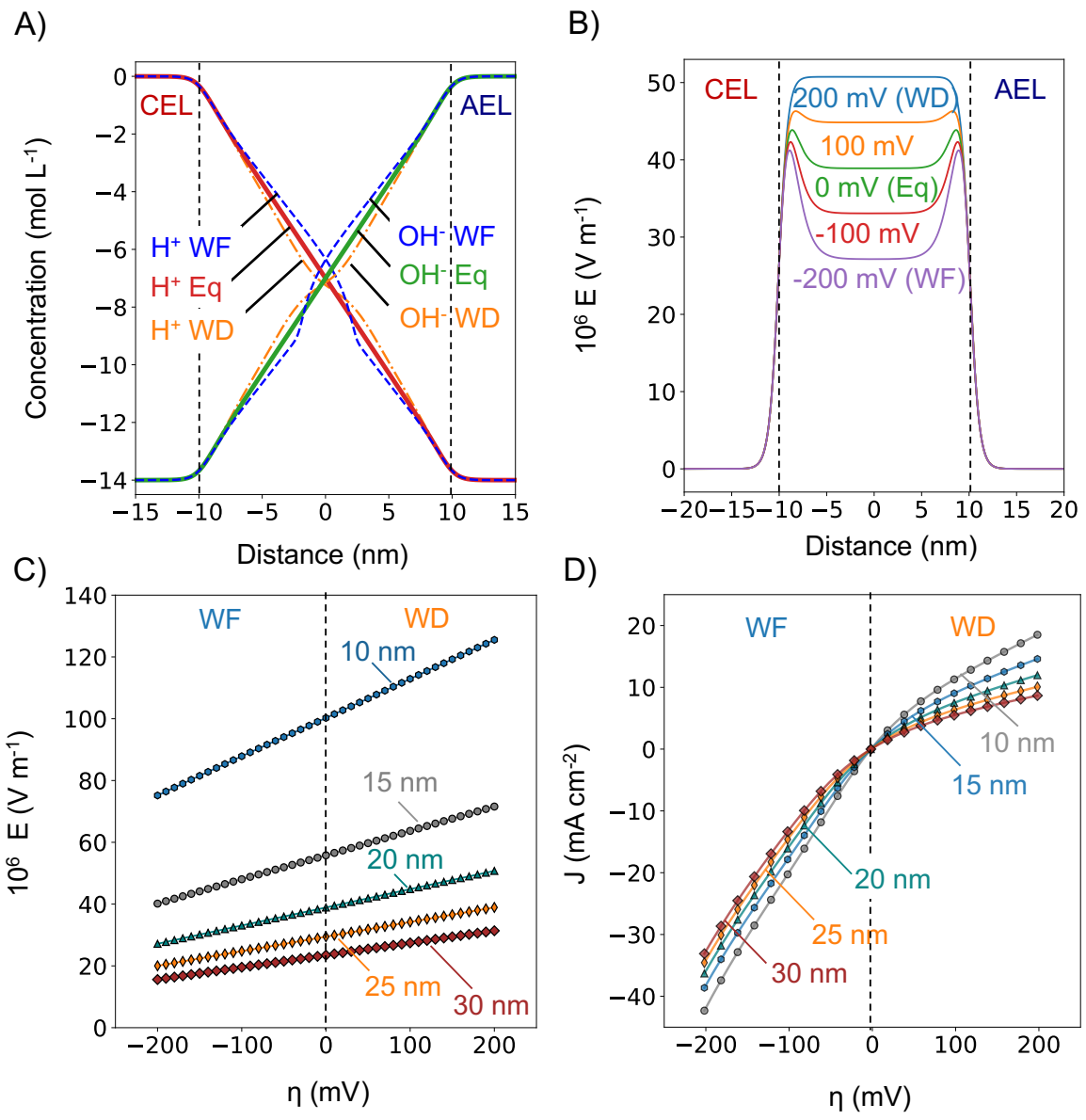

Supplementary Figure 18. BPM model validation. A) The concentration profiles for H^+ and OH^- under 100 mV WD/WF bias only display slight variations from electrochemical equilibrium. B) The electric field under WD bias (100, 200 mV) and WF bias is relatively uniform across the junction, except for the junction-AEL and junction-CEL interface. The total electric field is shown. The net electric field (subtracting the equilibrium electric field) changes (almost symmetrically) when switching polarity and driving WF. C) Electric field strength for different junction thicknesses. D) Polarization curves for different junction thicknesses.

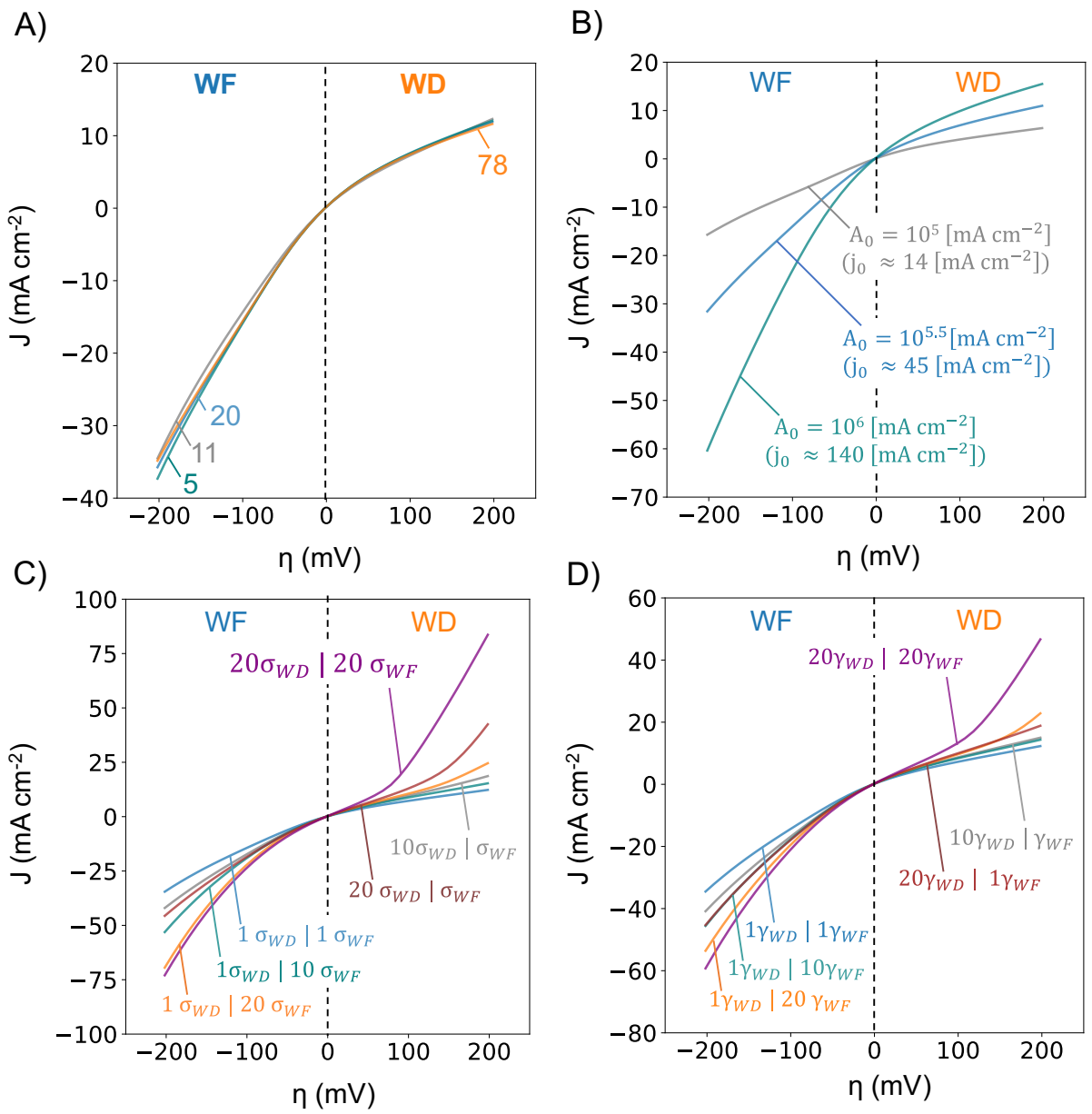

Supplementary Figure 19. Simulated polarization curves with different parameters. A) Changing the dielectric constant does not substantially change the polarization curve, as the overpotential drops almost uniformly over the junction thickness and the electric field action is not further fine-tuned in this simple model (Supplementary Figure 18A and B). Despite this simplification, the polarization curves match the experimental trends qualitatively and almost quantitatively, which validates our approach and further indicates that the potential drop is in fact acting over an extended region inside the junction, instead of being spatially confined as in previous models to obtain much larger electric fields. B) Changing the pre-exponential factor impacts WF currents more strongly than WD currents, due to the larger rates caused by increasing proton and hydroxide concentrations inside the junction. j_0 is shown for E_A = 21 kJ mol^{-1} and 25 ºC. C) Impact of the introduced susceptibility parameter σ_{WD} of the activation energy E_A and (D) γ_{WD} for the pre-exponential factor A (see Supplementary Note 4).

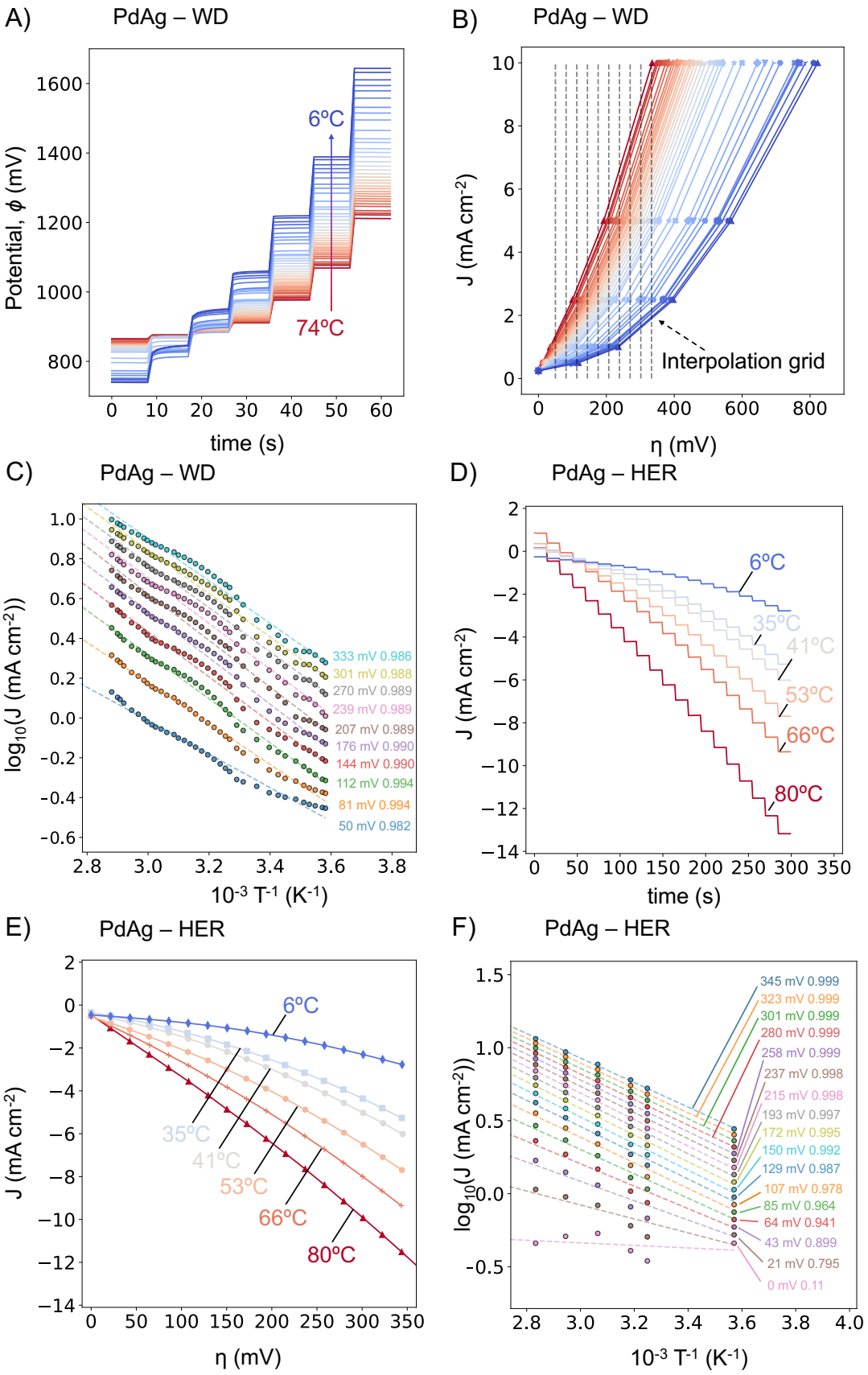
A)
PdAg – WD
Potential, ϕ (mV)
time (s)
6ºC
74ºC
B)
PdAg – WD
J (mA cm-2)
η (mV)
Interpolation grid
C)
PdAg – WD
log10(J (mA cm-2))
10-3 T-1 (K-1)
333 mV 0.986
301 mV 0.988
270 mV 0.989
239 mV 0.989
207 mV 0.989
176 mV 0.990
144 mV 0.990
112 mV 0.994
81 mV 0.994
50 mV 0.982
D)
PdAg – HER
J (mA cm-2)
time (s)
6ºC
35ºC
41ºC
53ºC
66ºC
80ºC
E)
PdAg – HER
J (mA cm-2)
η (mV)
6ºC
35ºC
41ºC
53ºC
66ºC
80ºC
F)
PdAg – HER
log10(J (mA cm-2))
10-3 T-1 (K-1)
345 mV 0.999
323 mV 0.999
301 mV 0.999
280 mV 0.999
258 mV 0.999
237 mV 0.998
215 mV 0.998
193 mV 0.997
172 mV 0.995
150 mV 0.992
129 mV 0.987
107 mV 0.978
85 mV 0.964
64 mV 0.941
43 mV 0.899
21 mV 0.795
0 mV 0.11

Supplementary Figure 20. Measurements of bipolar junction and HER kinetics at 0.1 M KOH-PdAg interface. A) Chronopotentiometry at different temperatures where the currents are set by the two counter electrodes in both compartments and the potential is measured between an Ag/AgCl reference electrode and the PdAg membrane. B) Polarization curves for WD potentials after subtracting the open-circuit potential. An extrapolation grid is used to extract currents at fixed potentials. C) Bias dependent Arrhenius analysis to extract pre-exponential factor and activation energy. D) Regular temperature-dependent HER kinetics on same PdAg foil. E) Temperature-dependent polarization curves after correction of the equilibrium potential. F) Arrhenius analysis for HER on PdAg.

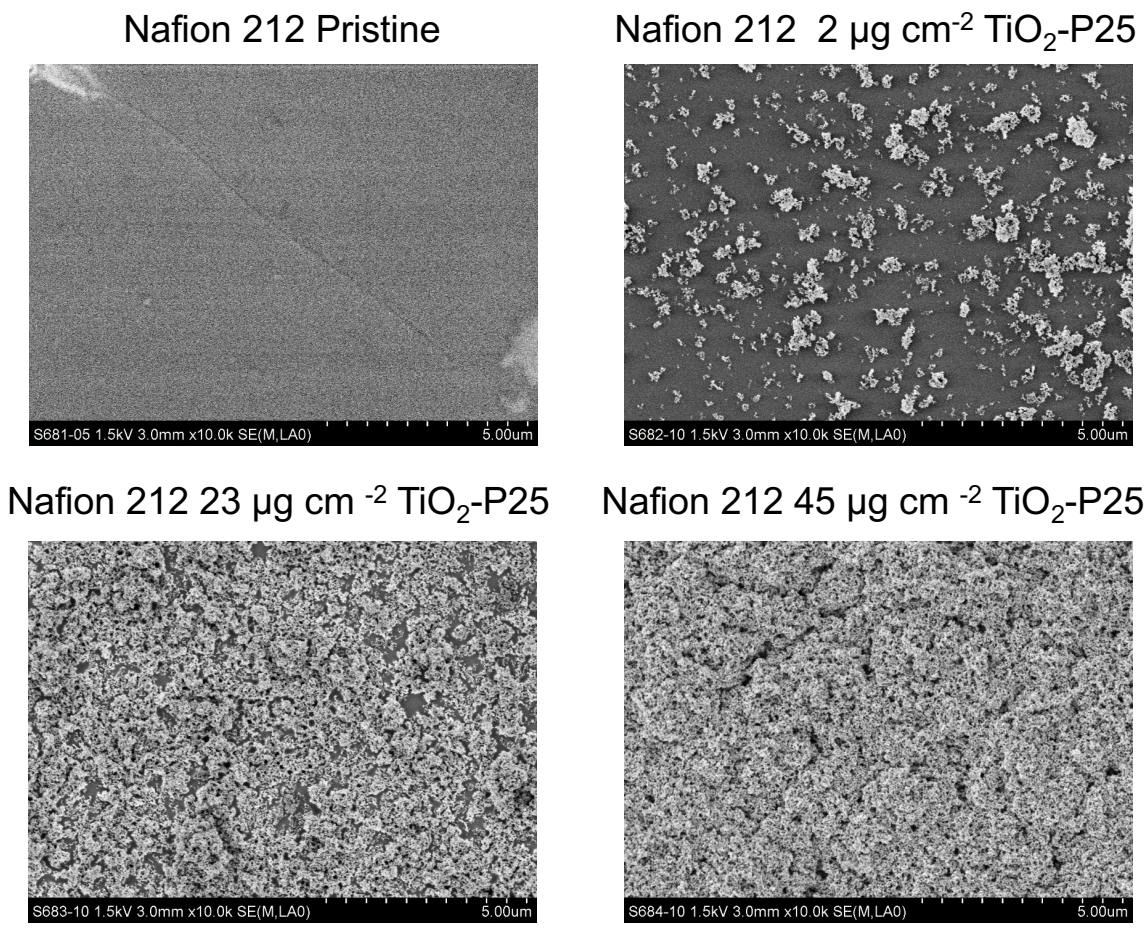

Supplementary Figure 21. SEM images of spray-coated Nafion 212 with different Loadings of TiO_2-P25. A) Without TiO_2 as reference. B) For low metal oxide loadings, spray-coating related cluster formation is apparent. However, the junction kinetics can be extracted accurately due to the overall low junction thickness between the mechanically compressed AEL and CEL that minimizes mass transport losses. C) Increasing catalyst loadings lead to increasing membrane coverage and even higher kinetics, however, at the expense of increasing the effective junction thickness. As a result, activated ion surface transport over extended nanoparticle beds can influence the extracted kinetics. D) For very high loadings, extracting E_A and A accurately is very challenging.

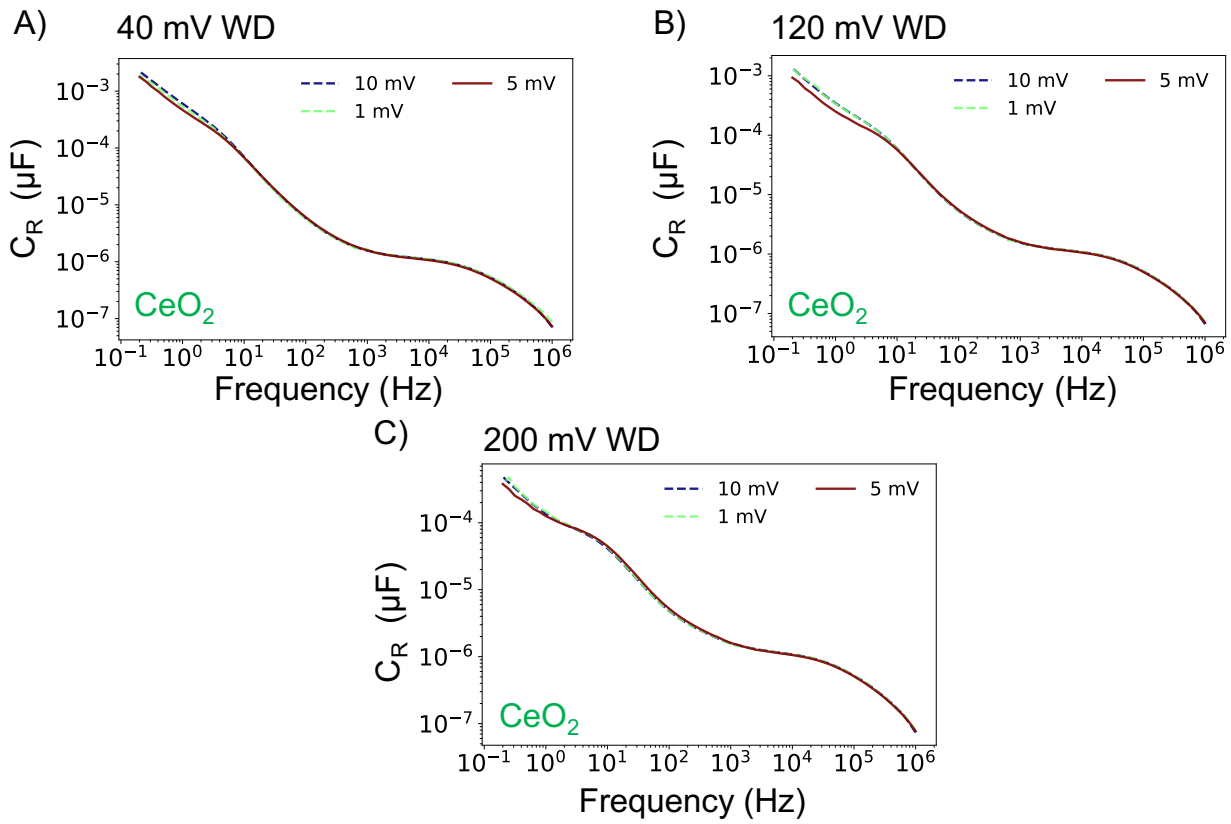

Supplementary Figure 22. Real capacitance extracted from impedance performed at different amplitudes. A-C) Impedance at different excitation amplitudes can be used to test for mass transport limitations. As evident here, we did not observe any appreciable changes, further supporting the absence of any substantial mass transport limitations (see Supplementary Note 1).

Supplementary Table 1. Comparison between our ion solvation model and a typical BPM model based on Onsager's 2nd Wien Effect.

	Ion Solvation Model	Onsager's 2nd Wien Effect Model
Description	WD and WF reactions are charge transfer reactions that involve interfacial ion (de)solvation following regular Arrhenius rate laws.	Based on Onsager's observations of conductivity deviations from Ohm's law for strong electric fields in weak electrolytes. Equations are from[9].
Main Equations	$j_{WD} = c_{H_2O}\left(A_{0_{WD}} + \gamma_{WD}\,\eta\right) \times \exp\left(\frac{-E_{a_{WD}} + \sigma_{WD}\,F\,\eta}{R\,T}\right)$ $j_{WF} = -c_{OH^-}c_{H^+}\left(A_{0_{WF}} - \gamma_{WF}\,\eta\right) \times \exp\left(\frac{-E_{a_{WF}} - \sigma_{WF}\,F\,\eta}{R\,T}\right)$ $j = j_{WD} - j_{WF}$ $R_{WD/WF} = \frac{j}{l_{junction}F}$	$\frac{k_{WD}(E)}{k_{0_{WD}}} = \left(\sum_{m=0}^{\infty}\frac{1}{m!\,(m+1)!}(2\beta E)^m\right) \times \cosh(\tau\beta E)\cosh(\tau)^{\beta E}$ $\tau = -0.28\ln(\cosh(0.235\sigma)) + 5.72\sigma^2$ $\sigma = \frac{0.58\,nm}{2l_b}; \quad l_b = \frac{eF}{8\pi\varepsilon_{H_2O}RT}$ $\frac{k_{WF}(E)}{k_{0_{WF}}} = 1 + \frac{1-\exp\left(-\frac{1}{\sigma}\right)}{2} \times \left(\sigma^2\beta E + (4.97\sigma)\frac{\sinh(0.0835\sigma\beta E)}{\cosh^2(0.0835\sigma\beta E)}\right)$ $\beta E = \frac{l_b F}{2.9\,RT}E$
Parameters	E_a, A, σ, γ, $l_{junction}$ (experimentally determined/ motivated)	β, τ, σ, l_b, -0.28, $\cosh(0.235\sigma)$, $5.72\sigma^2$, $0.58\,nm$, (4.97σ), $\sinh(0.0835\sigma\beta E)$, $\cosh^2(0.0835\sigma\beta E)$, 2.9 (see row above)
Remarks	Describes interfacial (de)solvation and WD/WF *via* bias-dependent E_a and A. Regular Arrhenius rate laws and Nernst Planck transport. Potentially applicable not only in BPMs, but also electro - and bio-chemistry in general.	Large range of experimentally inaccessible tuning parameters (see above). Both $k_{WD}(E)$ and $k_{WF}(E)$ increase with the electric field in WD direction.

Supplementary Table 2. Other parameters used in the COMSOL Multiphysics simulations.

General Description			
Parameter	Value	Unit	
T	25	ºC	Room temperature
ε_0	$8.85 \cdot 10^{-12}$	F m^{-1}	Dielectric permitivity of vacuum
F	96485	C mol^{-1}	Faraday's Constant
R	8.314	J K^{-1} mol^{-1}	Ideal Gas Constant
L_{char}	0.58	Nm	Hyperbolic tangent slope from bond distance O-H[9].
Geometry			
$l_{junction}$	20	nm	BPM Junction catalyst layer thickness. Assumed from a TiO_2-P25 monolayer.
CEL thickness	50	µm	Nafion 212
AEL thickness	25	µm	PiperION A25
AEL_{limit}	+10	nm	AEL-Junction interface from junction center
CEL_{limit}	-10	nm	CEL-Junction interface from junction center
Membrane Space Charge			
Parameter	Value	Unit	Description
AEL_{Cfix} CEL_{Cfix}	1000	mol m^{-3}	Fixed charge density of the membranes. Chosen as 1 (mol/L) for simplicity.
Dielectric constants			
$\varepsilon_M, \varepsilon_J$	11		For membranes and used for junction as well for simplicity. Obtained as the calculation for a mixture of water-dioxane[9].
Diffusion Constants			
D_{H+}^{j}	$6.96 \cdot 10^{-9}$	m^2 s^{-1}	Diffusion constant of H^+ in water
D_{H+}^{M}	$4.96 \cdot 10^{-9}$	m^2 s^{-1}	Diffusion constant of OH^- in water
D_i^M	$6.3 \cdot 10^{-10}$	m^2 s^{-1}	Calculated assuming 20 mS cm-1 given the membrane exchange capacity and kept identical for simplicity.
Reactivity Constants			
K_w (25 ºC)	10^{-8}	mol^2 m^{-6}	Water auto-dissociation constant
k_r	$1.38 \cdot 108$	m^2 $s^{-1}mol^{-1}$	Free water recombination constant[9].
k_f	1.3	mol m^3 s^{-1}	Free water dissociation constant[9].
A_0	$10^{5.6}$	mA cm^{-2}	Motivated by experiments.
E_{a_0}	21	kJ mol^{-1}	Motivated by experiments.
σ_{WD}, σ_{WF}	10^{-5}	C $m^{-1}mol^{-1}$	Susceptibility of E_a to the electric field. Motivated from experiments.
γ_{WD}, γ_{WF}	10^{-2}	S m^{-1}	Susceptibility of A to the electric field. Motivated from experiments.

Supplementary Table 3. Spray-Coating Calibration.

Measurement	Wafer w_0 (g)	Wafer w_f (g)	Difference (mg)	TiO_2 w_0 (mg)	Retaining Coefficient
1	2.27994	2.28030	0.36	2.01	0.18
2	2.33543	2.33596	0.53	2.05	0.26
3	2.27974	2.28032	0.58	1.99	0.29
4	2.27976	2.28045	0.69	2.16	0.32
5	2.33572	2.33606	0.34	2.04	0.17
6	2.27975	2.28037	0.62	2.00	0.31
7	2.28018	2.28054	0.36	2.08	0.17
Total Average	**0.24 ± 0.06**				

Supplementary References

1. Schalenbach, M. *et al.* Physicochemical Mechanisms of the Double-Layer Capacitance Dispersion and Dynamics: An Impedance Analysis. *J. Phys. Chem. C* **125**, 5870–5879 (2021).
2. He, Z., Chen, Y., Santos, E. & Schmickler, W. The Pre-exponential Factor in Electrochemistry. *Angew. Chemie Int. Ed.* **57**, 7948–7956 (2018).
3. Chen, L., Xu, Q. & Boettcher, S. W. Kinetics and mechanism of heterogeneous voltage-driven water-dissociation catalysis. *Joule* 1–32 (2023) doi:10.1016/j.joule.2023.06.011.
4. Pecina, O. & Schmickler, W. A model for electrochemical proton-transfer reactions. *Chem. Phys.* **228**, 265–277 (1998).
5. Giesbrecht, P. K. & Freund, M. S. Investigation of Hydrogen Oxidation and Evolution Reactions at Porous Pt/C Electrodes in Nafion-Based Membrane Electrode Assemblies Using Impedance Spectroscopy and Distribution of Relaxation Times Analysis. *J. Phys. Chem. C* **126**, 132–150 (2022).
6. Onsager, L. Deviations from Ohm's Law in Weak Electrolytes. *J. Chem. Phys.* **2**, 599–615 (1934).
7. Mafé, S. & Ramírez, P. Electrochemical characterization of polymer ion-exchange bipolar membranes. *Acta Polym.* 234–250 (1997) doi:https://doi.org/10.1002/actp.1997.010480702.
8. Giesbrecht, P. K. & Freund, M. S. Recent Advances in Bipolar Membrane Design and Applications. *Chem. Mater.* **32**, 8060–8090 (2020).
9. Bui, J. C., Corpus, K. R. M., Bell, A. T. & Weber, A. Z. On the Nature of Field-Enhanced Water Dissociation in Bipolar Membranes. *J. Phys. Chem. C* **125**, 24974–24987 (2021).
10. Hurwitz, H. D. & Dibiani, R. Experimental and theoretical investigations of steady and transient states in systems of ion exchange bipolar membranes. **228**, 17–43 (2004).
11. Schmickler, W. & Santos, E. *Interfacial Electrochemistry*. (Springer Berlin Heidelberg, 2010).
12. Santos, E., Quaino, P. & Schmickler, W. Theory of electrocatalysis: Hydrogen evolution and more. *Phys. Chem. Chem. Phys.* **14**, 11224–11233 (2012).
13. Gileadi, E. Problems in interfacial electrochemistry that have been swept under the carpet. *J. Solid State Electrochem.* **15**, 1359–1371 (2011).
14. Guidelli, R. *et al.* Defining the transfer coefficient in electrochemistry: An assessment (IUPAC Technical Report). *Pure Appl. Chem.* **86**, 245–258 (2014).
15. Boettcher, S. W. *et al.* Potentially Confusing: Potentials in Electrochemistry. *ACS Energy Lett.* **6**, 261–266 (2021).